VILNIUS UNIVERSITY

FACULTY OF PHYSICS

LASER RESEARCH CENTER

Aleksandras Kondratas

BOTTOM-UP PROCESSING OF GLASS USING MHz/GHz BURSTS OF ULTRASHORT LASER PULSES

Master‘s thesis

Study program – laser technology

Student	Aleksandras Kondratas
Allowed to defend	2026-05-22
Work supervisor	Dr. Juozas Dudutis
Reviewer	Dr. Simas Butkus
Consultant	Dr. Vytautas Jukna
Center director	Dr. Dalia Kaškelytė

Vilnius 2026

Contents

Introduction

The growing demand for miniaturization in electronic devices, medical technologies, and 5G systems has increased the need for advanced fabrication methods that can also reduce manufacturing costs [1]. Through-glass vias (TGVs) are attractive for such applications because they exhibit low parasitic capacitance, high mechanical strength, and tuneable thermal expansion properties through modification of the glass composition [1]. Metal-filled vias are used to form interposers required for the three-dimensional integration of Micro-Opto-Electro-Mechanical Systems (MOEMS) [2]. However, tapered TGVs introduce higher signal losses [1, 2], which is a common limitation of many existing TGV fabrication techniques [1, 3, 4]. In addition, high-aspect-ratio TGVs and more complex cavity geometries are needed for applications such as laser wakefield accelerators [5] and microfluidic systems [6]. One promising approach for producing taper-free structures is bottom-up laser drilling, which is investigated in this study.

In bottom-up drilling, the laser beam is focused on the bottom surface of the sample, allowing ablation debris to be expelled without obstructing the optical path [7]. This reduces beam shielding and enables the fabrication of deeper cavities and TGVs compared to conventional top-down drilling methods [8]. Furthermore, because the ablation conditions remain nearly constant throughout the process, channels with parallel sidewalls can be produced.

Femtosecond laser pulses cause a rapid increase in electron temperature while transferring minimal energy to the lattice. The absorbed energy is subsequently transferred to the lattice over several picoseconds, leading to material sublimation with a minimal heat-affected zone (HAZ) [9]. Sublimation-based ablation requires relatively high energy input. The use of laser bursts allows us finer control of energy deposition into the material.

Burst modes consist of groups of ultrashort laser pulses with intra-burst repetition rates ranging from several tens of MHz to a few THz, while the burst trains themselves are delivered at repetition rates from kHz to several MHz. The initial pulses within a burst heat the material and generate defects, reducing the ablation threshold for subsequent pulses. GHz bursts operate on timescales comparable to thermal diffusion [10] and are less influenced by plasma-induced disturbances [11]. As a result, GHz burst processing is generally more efficient than MHz burst processing, although this often comes at the cost of reduced surface quality. In dielectric materials, increasing the number of pulses within a GHz burst can alter the ablation mechanism to surface cracking and the ejection of micron-scale particles similar to ablation with nanosecond pulses.

The aim of this work was to investigate bottom-up processing of fused silica glass using various ultrashort pulse laser burst regimes. Objectives were to investigate (I) milling efficiency and rate of small diameter holes (≈100 μm) using MHz, GHz bursts, different GHz forms (rising, flat-top and falling), burst in a burst; (II) milling quality (surface damage and sidewall roughness); (III) milling of hole matrices; (IV) airflow-assisted milling for debris removal; (V) to fabricate through glass vias, (VI) complex shape channels, and (VII) compare burst-mode and nanosecond laser bottom-up processing.

This work was prepared at Center for Physical Sciences and Technology (FTMC), Department of Laser Technologies, Laser Microfabrication Laboratory.

1. Theory part

1.1. Absorption mechanisms in transparent materials

Linear absorption occurs when a single photon promotes an electron to a higher energy state. In dielectrics and semiconductors, photons of higher energy than bandgap, can be directly absorbed by the material resulting in energy transfer. Bandgap is defined as energy difference between valance and conduction bands. The bandgap of fused silica is around 9 eV. Additionally, materials can have defects which result in enhanced absorption. Defects can be created during laser-material interaction.

Alternatively, absorption can occur with photons which have energy lower than the bandgap when light intensity is high enough. This is called nonlinear absorption and can result in multiphoton absorption, electron tunnelling, or avalanche ionisation (Figure 1). Multiphoton absorption occurs when multiple photons are absorbed at the same time and their combined energy exceeds that of the material bandgap. This can be achieved in a few configurations, where the photons are identical or have different energies. The higher the number of photons that are needed to overcome the bandgap the lower the probability is for the process to occur. Therefore, multiphoton absorption as well as other nonlinear phenomenon are highly dependent on the laser radiation intensity [12]. Tunnelling occurs when an electron passes through a potential barrier in an electric field. This happens because a strong electric field distorts the potential field in such a way that lowers the energy the electron must overcome. From Keldysh model we see that tunnelling depends on electron velocity which can be calculated by $\sqrt{E_g/m}$. This means that tunnelling occurs at frequencies up to those determined by instantaneous field strength [13]. Avalanche ionization occurs when electrons are accelerated back into the atom through inverse Bremsstrahlung absorption resulting in collision which frees an additional electron [14]. The number of electrons generated via avalanche ionization grow exponentially with time, however, some free carriers are required for the process to start. Initial electrons usually come from defects or are created by processes mentioned above.

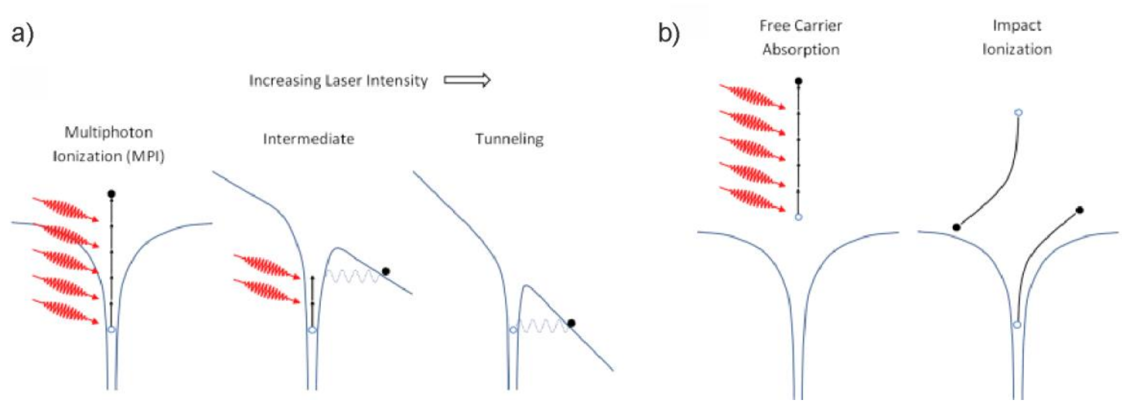

Figure 1. a) Multiphoton absorption, electron tunnelling, and b) avalanche ionisation schemes. Adapted from [15], with permission from Elsevier.

A parameter which can determine whether multiphoton or tunnelling ionisation will occur is adiabaticity γ, equation (1), which is described by Keldysh model [13]. Here E (equation 2) and ω are the strength and the frequency of the electric field, m is the effective mass of electron-hole pair, E_g is material bandgap, c is the speed of light, ε_0 is vacuum permittivity, I is light intensity, and e is the electron charge. When γ is significantly larger than 1 multiphoton absorption occurs, when it is close to 1 both multiphoton absorption and tunnelling can be observed, otherwise tunnelling is prevalent.

$$\gamma = \frac{\omega\sqrt{2mE_g}}{eE}. \tag{1}$$

$$E = \sqrt{\frac{2I}{c\varepsilon_0}}. \tag{2}$$

For 515–530 nm wavelength 4 photons are needed to overcome fused silica bandgap (~9 eV). In this work, adiabaticity γ is significantly smaller than 1, indicating that the primary mechanism of ionisation is tunnelling.

1.2. Nonlinear beam propagation in media

Refractive index of the material depends on the laser intensity (equation 3). Here, n_2 is nonlinear refractive index and I is intensity. The centre of the Gaussian beam has higher intensity than the sides. This creates a gradient of refractive index which bends the beam wavefront similarly to a lens. Beam cannot be focused to infinitely small point because of plasma defocusing. Presence of free carriers results in reduction of refractive index which counteracts self-focusing. This occurs when critical power is reached resulting in beam collapse. Beam propagation can cycle through self-focusing and plasma defocusing, which results in a tightly focused beam which can propagate for a long distance [14]. Critical power is described by equation (4), here α is a constant related to beam profile (α = 3.77 for a Gaussian beam), λ is the wavelength of light, n_0 is linear refractive index. Critical power for self-focusing, in fused silica with 515 nm wavelength, is around 1.1 MW.

$$n = n_0 + n_2 I(r,t). \tag{3}$$

$$P_{cr} = \frac{\alpha \lambda_0^2}{8\pi n_0 n_2}. \tag{4}$$

1.3. Burst modes

Burst modes consist of multiple ultrashort pulses with intra-burst repetition rates on the order of MHz, GHz, or THz, resulting in temporal separation of picoseconds to few tens of nanoseconds. For GHz and higher burst repetition rates, the time between pulses is short enough to allow for heat accumulation between pulses. As the number of pulses in a burst increases the ablation mechanism changes from sublimation to thermal cracking (Figure 2). Sublimation is less efficient because a single ultrashort laser pulse heats up the lattice above evaporation threshold temperature and excess energy contributes to larger heat-affected zone (HAZ) and increase in kinetic energy of ejected debris. M. C. Karse *et al.* [16] in 2016 demonstrated that working with high repetition rate burst increases milling efficiency because laser pulses ablate locally heated areas. With kHz to MHz repetition rates lattice has enough time to cool down between pulses, resulting in heat-affected zones even with fs pulses. With GHz repetition rates lattice is gradually heated up to threshold temperature, where the subsequent pulses result in efficient ablation.

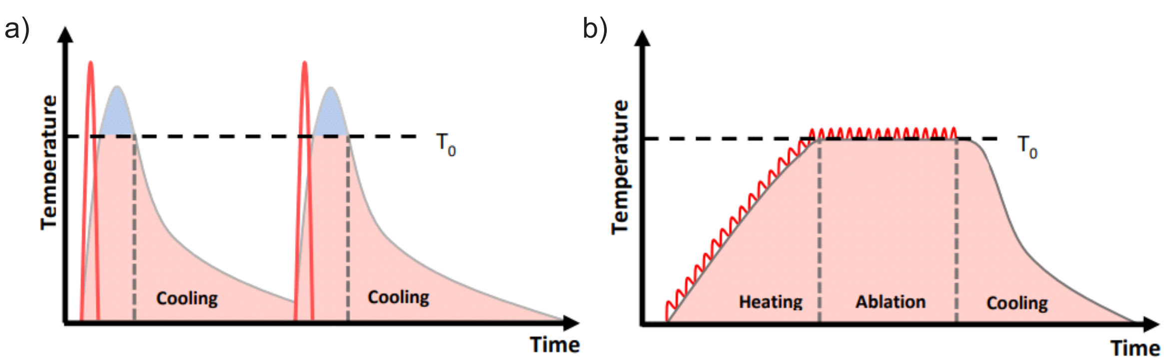

Figure 2. Representation of two-temperature model for a) single pulse and b) GHz burst ablation. Image by Pierre Balage [17], used under CC BY 4.0.

MHz bursts facilitate higher quality milling, especially for dielectric materials by reducing the probability of cracking [17]. MHz bursts offer higher milling efficiency than single pulses for glass ablation. Bursts offer flexibility by allowing control over energy deposition dynamics by controlling burst energy and repetition rate [17]. However, it is still challenging to control heat accumulation, requiring optimisation of many laser parameters. Additionally, for top-down ablation, burst repetition rate and intra-burst repetition rate should be optimised to avoid plasma shielding.

Pulses in a GHz burst mode arrive faster than heat diffusion time. This allows for subsequent pulses to interact with hotter material thus reducing the ablation threshold [18, 19]. Two temperature model (TTM) simulations show that lattice temperature increases with burst number but only if the burst separation time is close to the electron-lattice relaxation time of the material. Otherwise, TTM simulations showed increased temperature only for the second pulse in the burst with 50 ns pulse separation time. The heat-affected zone can be estimated with thermal diffusion equation $l_D = \sqrt{D_h \tau}$, where D_h is the thermal diffusivity and τ is the total burst duration. Optimal operation with burst regimes works with sub-threshold pulses. Therefore, intensities needed for Colomb explosion, one of the main mechanisms for classical ablation of dielectric materials, are not achieved. With GHz bursts, energy deposition time into the material increases from few hundred femtoseconds to nanoseconds. This results in higher heat accumulation. As the number of pulses in a burst increase, material removal method changes to cracking and particle ejection induced by thermal stress [20]. This effect is seen in brittle dielectrics. Such processing is inherently more efficient because energy is not used for the evaporation of the material.

In a study by P. Balage *et al.* [10], percussion drilling of soda-lime glass was done with GHz burst of various shape and constant burst energies, where they demonstrated a higher ablation rate with decrease in quality when using decreasing burst shape. A flat burst profile showed opposite qualities, while an increasing burst shape was reported to be an in-between of the two previous modes in terms of ablation rate and quality.

1.4. Top-down vs bottom-up drilling

Direct laser ablation, a top-down fabrication approach, can be used to machine glass samples with complex geometries, coatings, rough surface, or coloured compositions. In this process, ablation starts at the surface and proceeds downward, with material removed sequentially in layers. The resulting channels typically exhibit a V-shaped profile, as illustrated in Figure 3 a), where the inclination of the sidewalls defines the taper angle. This geometry arises from beam scattering and multiple reflections within the channel, which establish the initial wall angle based on the laser beam profile [21]. Employing a top-hat beam profile can reduce the taper angle, and previous studies have shown that this approach produces smoother surfaces than conventional Gaussian beams, with little to no decrease in milling efficiency [22].

The relatively low thermal conductivity of glass leads to the accumulation of stress gradients during ablation, which substantially restricts the achievable milling rate, particularly for thicker substrates. Moreover, redeposited ablation debris may remain on the surface and obstruct the incoming laser beam. Plasma shielding further contributes to energy loss, especially for short laser pulses, as electron–lattice energy transfer occurs over several to tens of picoseconds, while plasma dissipation typically takes place on the nanosecond timescale [23]. To mitigate these effects, airflow directed at the machining region can be used to remove debris and provide limited cooling [3, 24]. However, precautions must be taken to prevent particles from being blown onto the focusing lens or other optical components.

As an alternative, a bottom-up fabrication approach may be employed, in which the laser beam passes through the sample and is focused on the rear surface. In this configuration, ablated material is expelled from the backside, minimizing beam obstruction and reducing scattering effects along the optical path [7]. As a result, channels with greater depths can be achieved [8]. The sidewalls of the fabricated channels are nearly parallel because the milling conditions remain uniform for each ablated layer, except at the entrance and exit surfaces (Figure 3 b). Channels with complex geometry can be fabricated such as with decreasing then increasing diameter or channel formed not perpendicular to bottom surface [5]. However, this technique is limited to glass materials with sufficiently high optical transmission and a high-quality front surface finish [7].

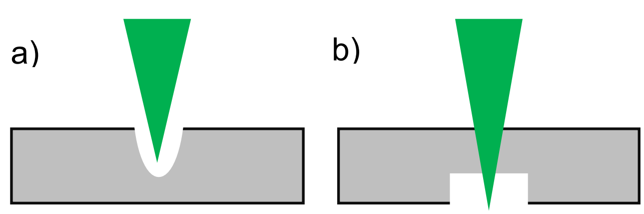

Figure 3. Laser milling strategies: a) top-down and b) bottom-up milling.

1.5. Fabrication technologies of through glass vias

TGV fabrication technologies can be divided into electrical and electro-chemical discharge machining, abrasive jet or mechanical machining, and laser-based, such as laser-induced chemical etching, top-down or bottom-up drilling.

Electrical discharge method (EDM) uses electrodes which generate an electrical discharge to locally liquify the material. Additional joule heating reduces viscosity resulting in material removal [25]. The processing time for a via is typically 0.2 – 0.5 s per discharge [1]. Multiple electrodes can be placed in a matrix resulting in simultaneous formation of many vias. However, the material thickness is limited to 100 – 500 µm resulting in 20 – 60 µm diameter vias with decreasing via diameter on the bottom side of the sample [1]. Workpiece is often submerged in a dielectric fluid (e.g. deionized water) which helps with cooling and material removal.

Electro-chemical discharge machining (ECDM) has the workpiece submerged in an electrolyte bath. High voltage on the tool electrode creates hydrogen bubbles which explode during discharge melting and vaporising the material. The electrolyte bath works to chemically dissolve and remove the debris from the working area. Vias created by ECDM depend on the tool electrode size and roughness [1]. However, processing is quite slow, average drilling rate is 3 µm/s. Minimum via diameter is limited to ~300 µm which is larger on the front size of the sample [1].

Abrasive jet machining (AJM) uses Al_2O_3, garnet, SiC, or diamond particles in a water/air/slurry jet, which can be used to process a wide variety of materials [1, 3]. Glass is processed by brittle erosion where the surface is cracked and subsequently removed. For glass drilling and cutting, Al_2O_3 is mostly used, composing up to ~8% of jet mass. Hole drilling speed with air jet is 0.1 – 32 µm/s, while in a slurry environment 0.6 – 4.4 µm/s [1]. Created holes or vias are around 4 times the size of the jet and can reach 300 µm diameter with aspect ratio of 5 [1]. AJM processing leaves a rough surface near drilled surface; this can be mitigated by using a mask, which can also reduce via diameter.

Mechanical drilling uses fast rotating drills which crack glass surface on contact. Resulting surfaces are usually rough, top surface chipping is around 50 µm, while bottom surface chipping is usually even larger. Aspect ratio varies from 0.3 to 4 for 0.13 mm to 4 mm depth holes. Typical drilling rate is ~5 µm/s [3].

Laser-induced chemical etching (LISE) uses ultrafast laser pulses to locally modify glass which is then selectively etched. Femtosecond laser pulses are used due to short interaction time reducing the heat-affected zone. Additionally, high laser intensity results in nonlinear absorption in transparent materials allowing for 3D structuring [4]. Femtosecond laser affected areas form nanograting structures and have increased internal stress which result in different chemical and physical properties. This is exploited for selective chemical etching, with up to few hundred times higher etching rate compared to unmodified glass [4]. Etching times are usually in the order of hours. Selectivity depends on laser scanning parameters and etchant [26]. Most used etchants are potassium hydroxide (KOH) and hydrofluoric acid (HF). Selectivity with KOH is higher than with HF, however, etching speed is typically slower. HF is highly hazardous to humans requiring strict safety protocols. Since etching can only start from the surface and progress to the desired structure, a taper is created near the surface [4, 25]. Bessel beams can be used to enhance the speed of fabrication. Due to their large focal depth (can be matched to the sample thickness), glass modifications can be done in a single shot [27].

Percussion top-down drilling with MHz, GHz bursts use laser burst focused to a single spot on the top side of the sample. The sample is then irradiated thousands of times with number of pulses in the burst typically ranging from 10 to 100 [28, 29]. Resulting cavities grow with number of pulses/bursts until saturation is reached. GHz bursts were demonstrated to be capable of achieving higher depth than MHz burst [28]. Additionally, it was demonstrated that increasing the number of pulses in the GHz regime results in higher depth channels with smoother side walls and minimal entrance chipping [28]. Cavity shape is not constant, there can be an increase in diameter after some depth, and end of drilling the cavity curves to the side and has decreased diameter. For longer depth channels there can be slight deviations in channel propagation [28]. To drill high quality through holes, a sacrificial layer is need or polishing off the depth with irregular cavity shape. P. Balage *et al.* [28] has demonstrated 3.7 mm depth cavities with 25 µm entrance diameter in soda lime glass using GHz bursts.

Submicrometric holes created with single-shot Bessel beams can have 200 – 800 nm diameters in thin substrates [30]. Bessel beams have high focal depths and small diameter of the central core, therefore, a submicrometric diameter line of material can be excited along the whole thickness of the sample in a single shot. Excited material turns to plasma which expands and is expelled from the formed hole. Repeatable high-speed fabrication of few micrometre diameter holes in 1 mm thickness silica glass was demonstrated with two shot setup using two different pulse duration lasers [31]. First picosecond pulse excites the material enhancing selective absorption for the second microsecond pulse.

1.6. TGV applications

Through glass vias offer lower parasitic capacitances compared to silicon, high mechanical strength, and glass composition can be modified to change thermal expansion coefficient [1]. Metal filled vias form the interposers, which are necessary for 3D integration of Micro-Opto-Electro-Mechanical Systems (MOEMS) [2]. Create connections for microfluidic elements. TGVs with a tapered hole experience higher signal loss [1, 2], which happens with a lot of TGV technologies [1, 3, 4].

Laser-plasma acceleration

Ultrashort laser pulses shot at a plasma target vibrates the plasma producing X-ray radiation. This happens because electrons are accelerated by the laser pulse and follow its oscillations producing betatron radiation. Increasing laser pulse energy and plasma density lower laser wakefield acceleration (LWFA) intensity threshold which facilitates the creation of tabletop X-ray sources [32]. This radiations' harmonic peaks can reach tens to hundreds of keV. Plasma characteristics can be tailored by fabricating micrometric nozzles for gas ejection. By customising the geometry of nozzle arrays, it is possible optimise the efficiency of betatron radiation depending on laser power, focusing depth, and required plasma density profiles.

Nozzle manufacturing from metals is time consuming and does not allow for complex, high aspect ratio holes. Stereolithography allows for fast manufacturing, however, post-processing is often required to open closed holes, and available materials are of moderate strength. An alternative material could be glass due to its hardness and available methods of manufacturing micro scale holes as discussed above.

Electronics packaging

Through glass vias have lower parasitic capacitance and better electrical properties compared to through silicon vias (TSV). Due to optical transparency of glass, it can be used in MOEMS. Other properties of glass which are useful for different sensors are shown in Figure 4. TGV connections are easier to make because they do not require an additional insulating layer on the inner walls as is done in TSVs. TGV chips can be 50% denser and two times thinner than vias made in ABF plastic [1].

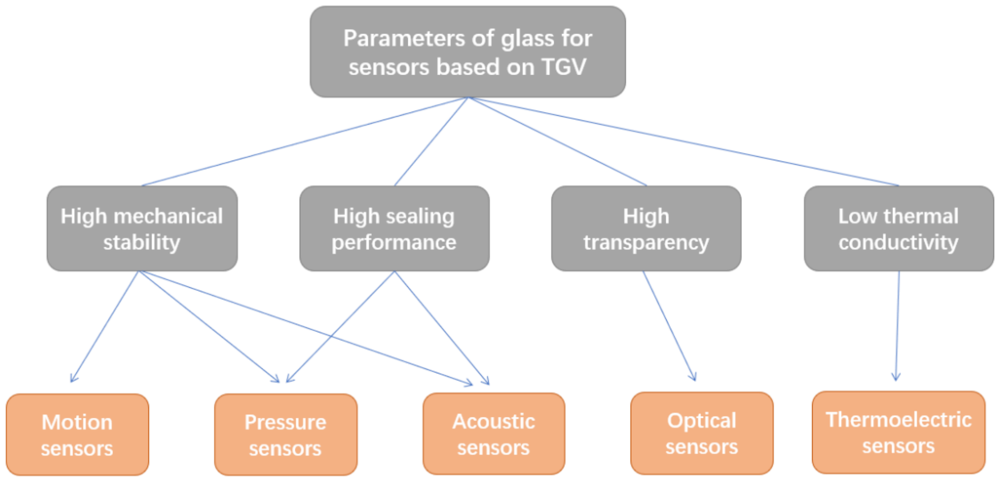

Figure 4. Glass parameters which are used for different sensors. Image by Chen Yu *et al*. [1], used under CC BY 4.0.

2. Experimental setup

Most of the experiments were done using a FemtoLux30 (Ekspla) laser which emits ~350 fs pulses measured at full-width-half-maxima (FWHM). Pulse duration depends on laser repetition rate and fluctuates by about 20 fs. The laser was operated at the central wavelength of 515 nm. This laser has MHz and GHz burst regimes with intra-burst repetition rate of ~50 MHz and 2.76 GHz, respectively. Another part was done with Atlantic 60 (Ekspla) laser which emits ~4 ns and ~11 ns pulses (FWHM) and operated at 532 nm central wavelength. The femtosecond laser was used unless nanosecond pulse duration was mentioned. The beam position in the X and Y axes was controlled by an excelliSCAN 14 (ScanLab) galvanometer scanner, while the sample position in the Z axis was changed with a motorized translation stage 8MVT120-25 (Standa). Milling features were kept in the centre of galvanometer field by moving the sample with translation stages. The XY movement between milling each feature was controlled with the ALS25020 (Aerotech) motion control platform. Processing was programmed and controlled with the Direct Machining Control (DMC, version 1.8.95) software. A zero-order air-spaced quarter-wave plate 464-4432 (Eksma

Optics) was placed before the galvanometer scanner to convert the linear polarization into circular. The femtosecond laser beam was focused on the sample via a 50 mm focal length telecentric f-theta lens S4LFT3060/292 (Sill Optics) to the radius of 3.4±0.1 μm at the 1/e^2 intensity level as measured by the Liu's method [33]. For this, chromium was ablated from a glass substrate with different pulse energies and resulting squared diameters (Figure 5) were fitted according to $D^2 = 2\omega_0 \ln(E/E_{th})$. Plotting energy in natural logarithm scale allows us to take the linear fit slope value k, from which beam radius at 1/e^2 intensity level can be calculated $\omega_0 = \sqrt{k/2}$. The principal scheme for bottom-up ablation is shown in Figure 6. The ablated particles were collected with an AD Oracle iQ (BOFA) fume extraction system working at 150 m^3/h.

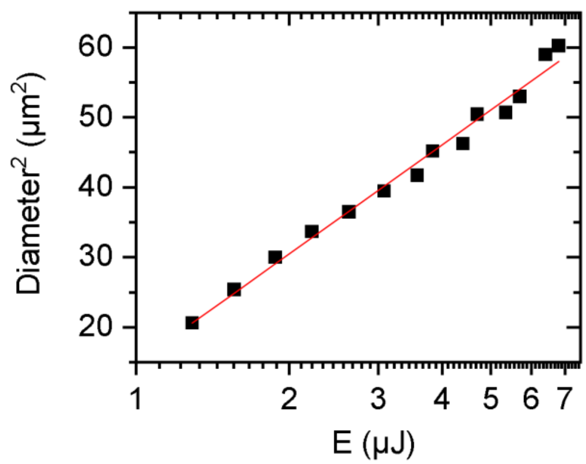

Figure 5. Ablated area diameter squared dependence on pulse energy. Red line is a linear fit.

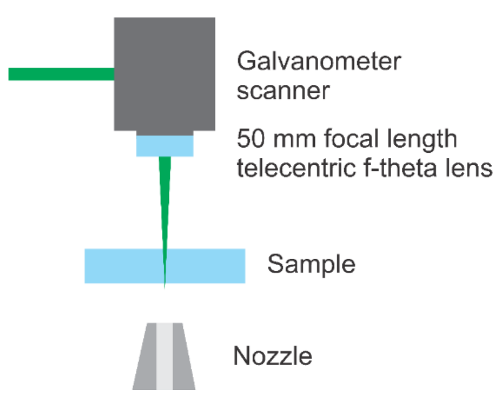

Figure 6. The principal scheme of bottom-up drilling.

Pulse durations of nanosecond laser were measured from oscilloscope data at FWHM (Figure 7). Femtosecond laser bursts were measured for first harmonic Figure 8. We can see that with form = 0 pulse intensity decreases for subsequent pulses in a burst with $N_{GHz} = 10$, however with $N_{GHz} = 28$ pulse intensity is mostly flat-top. Values for rising and falling burst forms resulted in very steep slopes which would be even steeper with second harmonic. After $N_{GHz} = 28$ the next available number of pulses is 56 and it has a complex form (Figure 8 b).

Nanosecond pulses in Figure 7 were measured with photo detector DET210 and oscilloscope TDS 2022 (Tektronix). GHz burst in Figure 8 were measured with high-speed detector D-15ir (Picometrix) and oscilloscope DPO72004C (Tektronix).

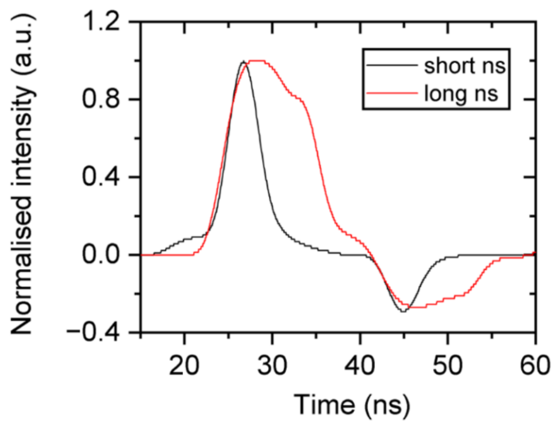

Figure 7. Oscilloscope measurements of nanosecond pulses. Measured at 532 nm wavelength.

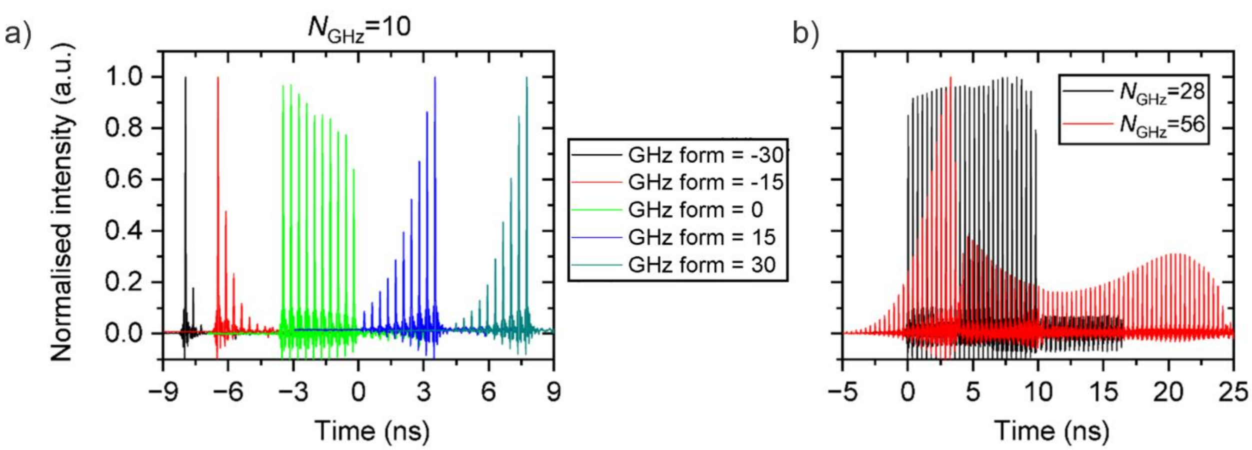

Figure 8. Oscilloscope measurements of burst regimes a) $N_{GHz} = 10$ burst with falling (negative) and rising (positive) burst forms and b) $N_{GHz} = 28$ and 56 with form = 0 (flat). Measured at 1030 nm wavelength.

In part of the experiments 6 different air nozzles were used with characteristics provided in Table 1. Exact internal nozzle design was not available for any nozzle. However, their orifices were assessed using an optical microscope. ALVA1 is a de Laval nozzle (Figure 9 a) which blows air at supersonic speed in a tight cone, the constricting diameter is 2.3 mm, it is 3.8 mm deep from the bottom side. Rotary nozzles SPNZ-A and B have a top which can freely rotate creating a more turbulent airflow, which could simulate pulsed airflow for enhanced debris removal (Figure 9 b and c). Rotary nozzles SPNZ-A and B differ in only the projection angle of the orifices. ARDADA1 has additional holes (1.5 mm in diameter) at the side which draws in surrounding air for increased airflow rate (Figure 9 d). Conical spray nozzle was the only other nozzle with a hole at the centre and had 8 surrounding orifices for higher projection angle. For clarity nozzles will be referred to by their type.

Table 1. Summary of applied airflow nozzles. Data was taken from [34] except orifice sizes, which were measured using an optical microscope. *Airflow was given at 0.3 MPa.

Nozzle type	de Laval	Rotary	Rotary	Amplify	Amplify	Conical spray
Nozzle name	ALVA1	SPNZ-A	SPNZ-B	ARDADA1	CERJET 8-008	ACNA1-20
Seller	MiSUMi					
Airflow rate at 0.5 MPa, L/min	250	160	160	300	235	195*
Projection angle, degree	16	24	90	*unspecified*	*unspecified*	20
Orifice size, mm	2.8	1.3	1.3	0.8	0.8	1

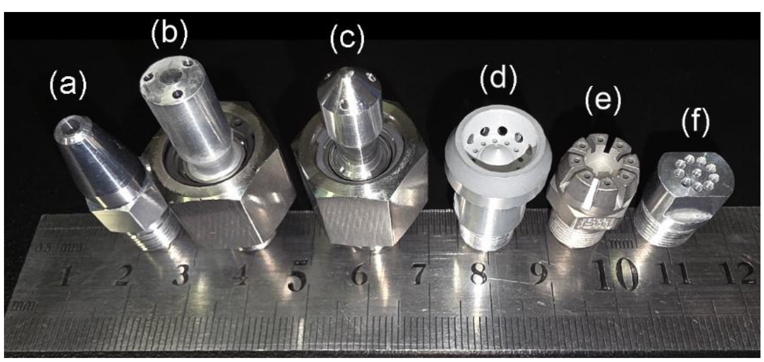

Figure 9. Image of nozzles: a) de Laval (ALVA1), b) rotary (SPNZ-A), c) rotary (SPNZ-B), d) amplify I (ARDADA1), e) amplify II (CERJET 8-008), f) conical spray (ACNA1-20).

3. Method

Fused silica (FS) samples with the outer dimensions of 152×152×6.3 mm^2 (rectangular), 75×75×12.8 mm^3 (rectangular), and 100 mm diameter × 1 mm (circular sample) were used in experiments. Approximately 100 µm diameter cavities were milled employing laser beam scanning trajectories, which are shown in Figure 10. Here, the distance between laser shots is noted as pitch p, the distance between concentric circles as spacing s. Scanning was repeated an additional number of times referred to as loops N_l, where each loop consisted of scanning concentric rings from the centre to outside and then going back to the centre. After each loop the sample was moved by a set distance (d_z) away from the scanner along the beam propagation coordinate. At the start of milling the laser beam was focused few hundred µm below the sample. Offset was found by milling cavities with different offset values, which was changed by a 50 µm step, until a value was found with which sample was not damaged. Milling was done with the lowest spacing and pitch values in the used matrix, d_z = 5 µm, and

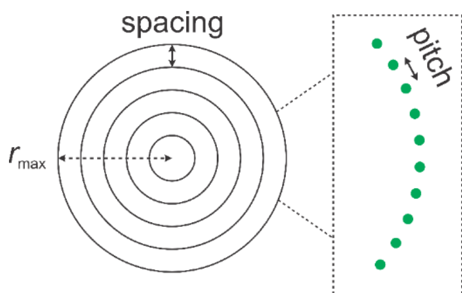

Figure 10. Scanning trajectories for cavity milling.

Matrices of cavities were milled to optimize d_z, pitch, spacing, burst energy, and number of pulses in a MHz or GHz burst. Cavity milling with each parameter combination was repeated 5 times to investigate process repeatability and acquire standard deviations (SD). In each matrix, the number of loops was changed from 15 to 60 by a step of 15 loops; d_z and burst energy were changed to 5 different values, while spacing and pitch to 3 values. The geometry of parameters changed in matrices is shown in Figure 11. After milling the whole set, MHz or GHz burst count, GHz burst form, or pulse duration was changed. Fundamental laser pulse (burst) repetition rate was set to ~100 kHz, but the actual repetition rate was reduced by 4 times to reduce scanning speed.

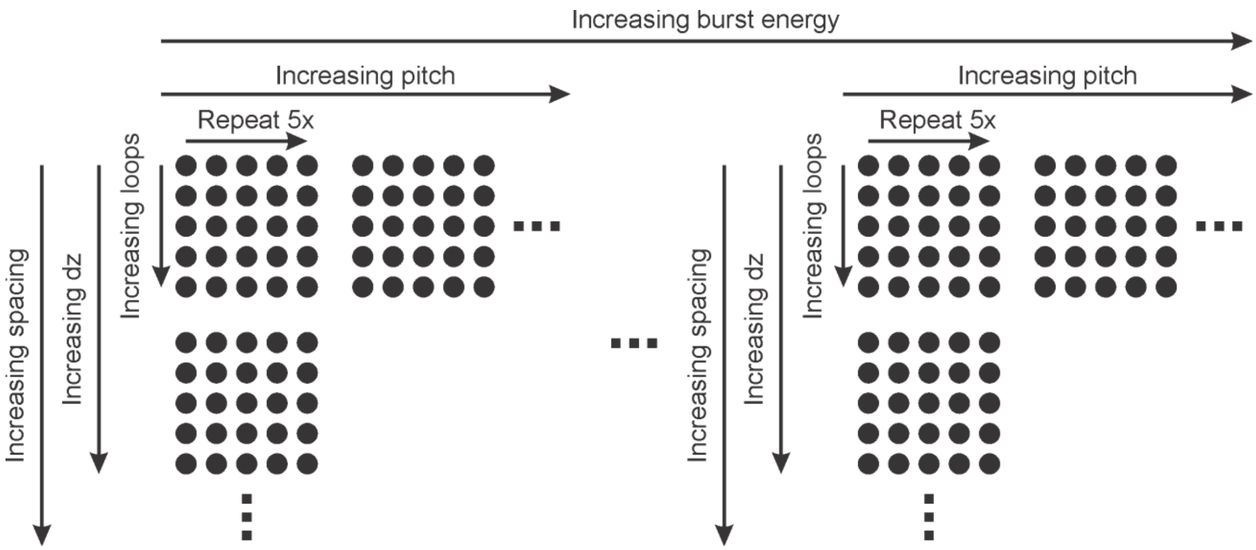

Figure 11. Milling logic of cavity matrices.

Total length of concentric rings is calculated as arithmetic sum C equation (5). For that we need the maximum radius r_{max} of the scanning rings, which was calculated as floored value of r_0/s multiplied by s (r_0 is 42 µm) equation (6). Total length C is then divided by pitch p and multiplied by 2 since each loop consisted of scanning concentric rings from the centre to outside and back, giving us the number of pulses per loop N_p (7). Drilled volume V (8) was divided by the number of pulses per loop N_p, burst energy E_b, and number of loops N_l to get efficiency η (9). Here, r_h is measured radius of milled cavity (~50 µm), d is the depth of cavity, and other variables were defined at the start of method section. In equations (8–12) depth, time, and number of loops are taken as the difference between two cavities milled with different number of loops, while all other milling parameters are the same, except for TGVs.

$$C = 2\pi s + 2\pi 2s + 2\pi 3s + \cdots + 2\pi r_{max} = \frac{\pi r_{max}(r_{max}+s)}{s} \tag{5}$$

$$r_{max} = \left\lfloor \frac{r_0}{s} \right\rfloor s \tag{6}$$

$$N_p = \frac{2\pi r_{max}(r_{max}+s)}{sp} \tag{7}$$

$$V = \pi r_h^2 d \tag{8}$$

$$\eta = \frac{V}{N_p N_l E_b} = \frac{spd}{2N_l E_b}\frac{r_h^2}{r_{max}(r_{max}+s)} \tag{9}$$

Linear milling rate v_l (µm/s) and material removal rate were calculated according to equation 10 and 11, respectively. Here t is the time it took to mill a cavity from the start of scanning to the end, including scanner jumps.

$$v_l = \frac{d}{t} \tag{10}$$

$$V_t = \frac{V}{t} \tag{11}$$

Uncertainty calculations for milling efficiency, milling rate, and material removal rate were done using equations (12–14), respectively. Here, n denotes which measurement was done (e.g. $d_n - d_{n-1}$ denotes the depth difference between two cavities milled with different number of loops).

$$\delta\eta = \eta\sqrt{\left(\frac{2\delta r_h}{r_h}\right)^2 + \left(\frac{\delta d_n}{d_n - d_{n-1}}\right)^2 + \left(\frac{\delta d_{n-1}}{d_n - d_{n-1}}\right)^2 + \left(\frac{\delta E_b}{E_b}\right)^2} =$$

$$\eta\sqrt{\left(\frac{2\delta r_h}{r_h}\right)^2 + \frac{\delta d_n^2 + \delta d_{n-1}^2}{(d_n - d_{n-1})^2} + \left(\frac{\delta E_b}{E_b}\right)^2}. \tag{12}$$

$$\delta v_l = \sqrt{\left(\frac{\partial v_l}{\partial d_n}\delta d_n\right)^2 + \left(\frac{\partial v_l}{\partial d_{n-1}}\delta d_{n-1}\right)^2} = v_l\sqrt{\frac{\delta d_n^2 + \delta d_{n-1}^2}{(d_n - d_{n-1})^2}}. \tag{13}$$

$$\delta V_t = V_t\sqrt{\left(\frac{2\delta r_h}{r_h}\right)^2 + \left(\frac{\delta v_l}{v_l}\right)^2}. \tag{14}$$

4. Sample characterisation

After laser processing, debris was blown off samples by compressed air and surface was cleaned with tissues soaked in acetone before further investigation.

An optical microscope Eclipse LV100NDA (Nikon) was used for taking pictures and to evaluate which cavities were milled successfully. Illumination was from the bottom of the sample, 10x magnification 0.3 NA objective (Nikon) was used.

For cavity depth measurements an optical profilometer S Neox (Sensofar) was used in active illumination focus variation regime. This regime can measure steep angles of ~86°. Measurements were done with 5x magnification, single field of view (FOV), 1.38 µm/pixel XY resolution.

To measure the sidewall roughness of channels, 20×5×6.3 mm^3 samples were prepared as shown in Figure 12 a). They had V-shaped indents to guide sample breaking. For each parameter set, 5 channels were milled ~350 µm above the breaking line (Figure 12 b). Sample were cleaned in an ultrasonic bath in water for ~15 min. The sample was broken with three-point breaking pliers (Figure 12 c). Channels were not milled collinearly with the breaking line, because breaking was non-uniform (Figure 12 d) which divided the channels between two pieces or failed to open them up. Broken samples were mechanically polished until channels were open (Figure 12 e). After polishing samples were cleaned in an ultrasonic bath in water for ~15 min. For roughness measurements optical profilometer S Neox (Sensofar) in the confocal regime was used. The objective with 20x magnification was used, pixel size was 0.34 µm, and measurement area was ~1.6×6.3 mm^2.

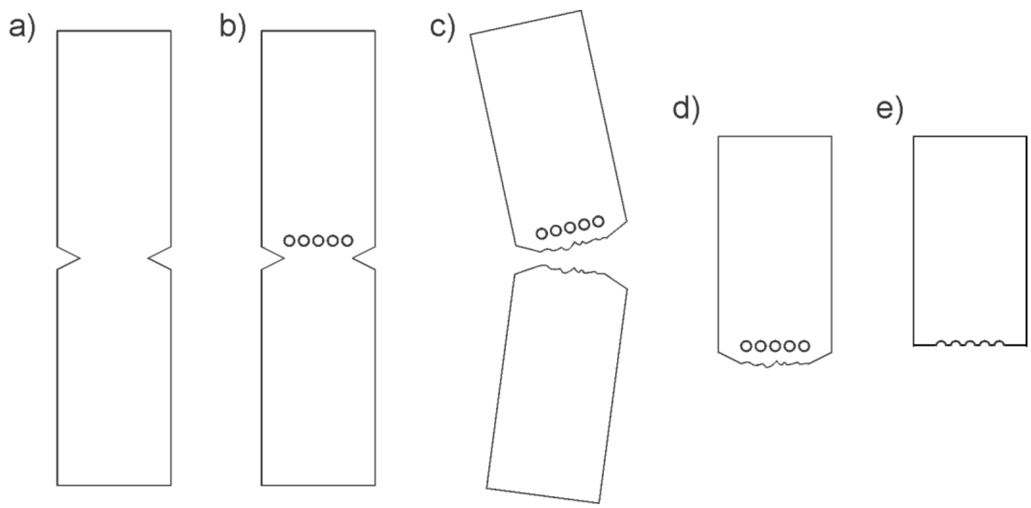

Figure 12. Sample for channel side wall roughness investigation. Sample with V-shape indents (a), channels milled near breaking line (b), broken sample (c-d), polished sample (e).

5. Results and discussion

5.1. Damage at stationary exposure

Liu method [33] was performed on the bottom surface of the sample to evaluate the damage threshold. Single-shot modifications were hardly visible and therefore not evaluated. This led to investigation of modifications with multiple shots. Modifications were evaluated using a microscope with a 100x magnification objective.

Figure 13 shows squared modification diameter dependence on pulse energy for 10 to 10000 pulses in a single spot when beam was focused to the bottom side of the sample. Single-shot top surface dependence which was used for beam diameter evaluation is plotted in blue for comparison (Figure 13 a). Using Liu method, beam diameter and ablation threshold values were acquired and noted in Table 2.

From 10 shots we can see that the beam radius is 2.6 times smaller than on the top surface. This indicated that beam experiences self-focusing inside the material. Additionally, peak power exceeds 1 MW for energies above 5 μJ. From 100 shots and more, beam radius returns to a similar size as on top surface. Likely due to accumulation of defects which increase the modification size.

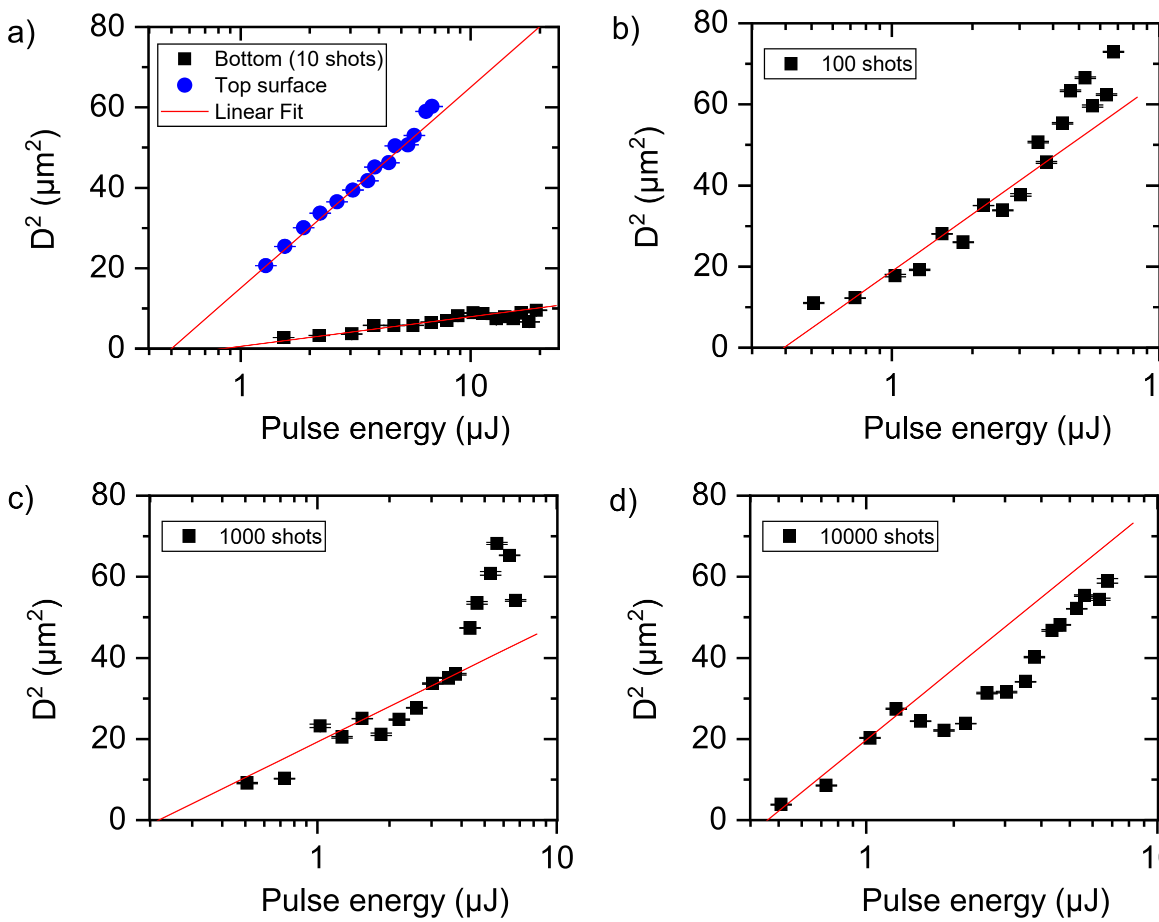

Figure 13. Liu method with different number of pulses a) top surface single shot and bottom surface 10 shots, b-d) bottom surface 100 to 10000 shots, respectively. Red line is linear fit. Error bars are standard deviation.

Table 2. Parameters acquired with Liu method. Error is standard deviation.

Shots	Surface	ω_0, µm	E_{th}, µJ	F_{th}, J/cm^2
1	Top	3.4±0.1	0.5	2.8±0.1
10	Bottom	1.3±0.1	0.85	33.9±2.5
100	Bottom	3.2±0.1	0.40	2.5±0.1
1000	Bottom	2.5±0.2	0.22	2.2±0.4
10000	Bottom	3.6±0.3	0.46	2.3±0.4

5.2. Initial scanning parameter optimisation

Matrices were milled with MHz burst of 2 – 5 and 10. Here, 50 loops were scanned for all cavities. Depths above 100 µm were achieved only with 2 pulses in a burst. Figure 14 a) shows how cavities milled with $N_{MHz} = 2$ looked. Darker spots around the circumference indicate debris that is stuck to the cavity walls. Additionally, microscope images that are darker have higher milled depth, but also more debris stuck inside. Figure 14 b) shows how a cavity full of debris appears fully black under diascopic illumination, while episcopic illumination shows the debris which is stuck inside the cavity. Most of the failed regimes appeared as shown in Figure 14 b). Volume modifications were made with little to no cracking. From these results we can conclude that MHz burst milling is inefficient or not possible for 100 µm diameter TGV drilling with the selected scanning parameters.

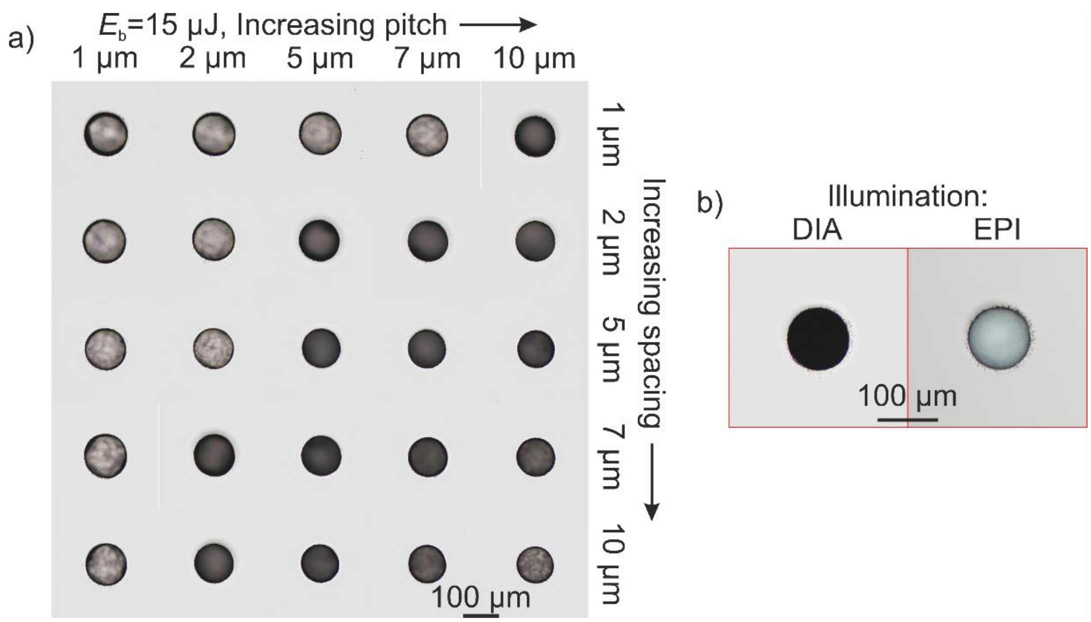

Figure 14. Microscope pictures of cavities milled with MHz burst count of 2, a) burst energy of 15 µJ, and b) burst energy of 5 µJ with diascopic (DIA) and episcopic (EPI) illumination.

5.3. Milling efficiency using various bursts regimes

GHz burst regimes

The highest d_z value for each parameter set (spacing, pitch, and burst energy) was found. The higher the multiplication of spacing, pitch, and d_z the higher the expected milling efficiency. Using this logic few spacing and pitch values were selected. Each measured point corresponds to the highest d_z with which milling succeeded. Cavity milling is successful when d_z is lower, however, when d_z is larger cavity milling fails. Failure manifests in cracking, low milled depth, or debris stuck inside the channel.

Milling without burst regime resulted in the worst efficiency which did not change much with pulse energy or different spacing and pitch values. Increasing number of pulses in the GHz burst resulted in higher maximum milling efficiency. For $N_{GHz} = 2 – 4$ the highest milling efficiency was with burst energy between 10 μJ and 20 μJ (Figure 15). In this range, the largest efficiency of 24.3±1.6 μm^3/μJ was achieved with $N_{GHz} = 4$, E_b = 15 μJ, s = 5 μm, p = 5 μm, d_z = 15 μm.

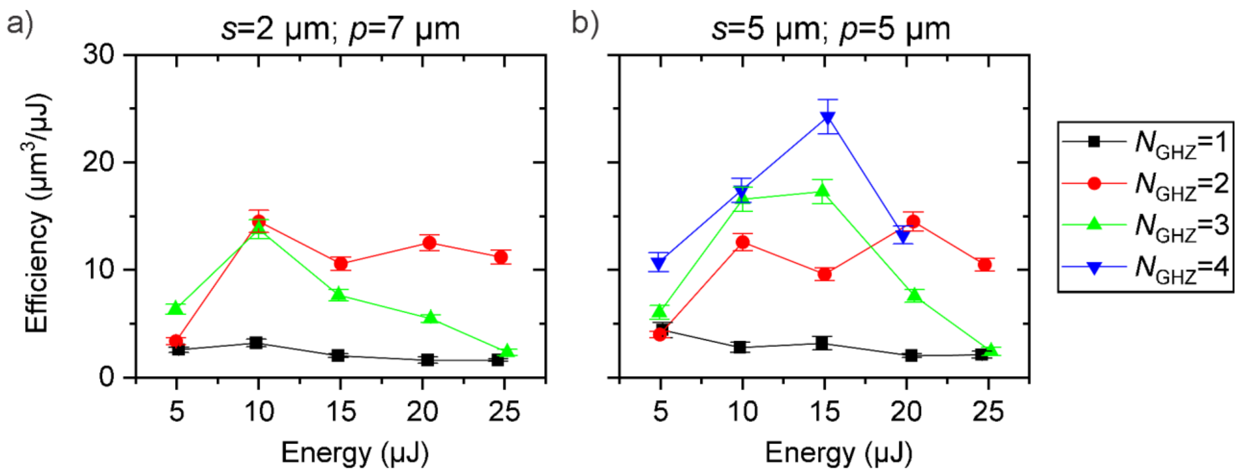

Figure 15. Milling efficiency dependence on energy when milling cavities with $N_{GHz} = 1 – 4$ and a) 2 μm spacing, 7 μm pitch, and b) 5 μm spacing, 5 μm pitch. Lines are for eye guidance. Error bars are uncertainty.

Figure 16 shows milling efficiency using a larger number of pulses per GHz burst (≥ 7). Increasing spacing and pitch values results in higher milling efficiency. However, when these values exceed the modification size, milling failed resulting in cracking. For most regimes the maximum efficiency was with burst energy of 10 μJ and below. The highest achieved milling efficiency was 201±15 μm^3/μJ when milling with $N_{GHz} = 21$, E_b = 5 μJ, s = 10 μm, p = 10 μm, d_z = 15 μm (Figure 16). There is a trend of decreasing milling efficiency with higher burst energy. Higher number of pulses in a GHz burst allow us to use higher spacing and pitch values which likely correspond to increased modification size. However, with very long bursts the interaction time becomes too long for some pulses to contribute to heating of the material.

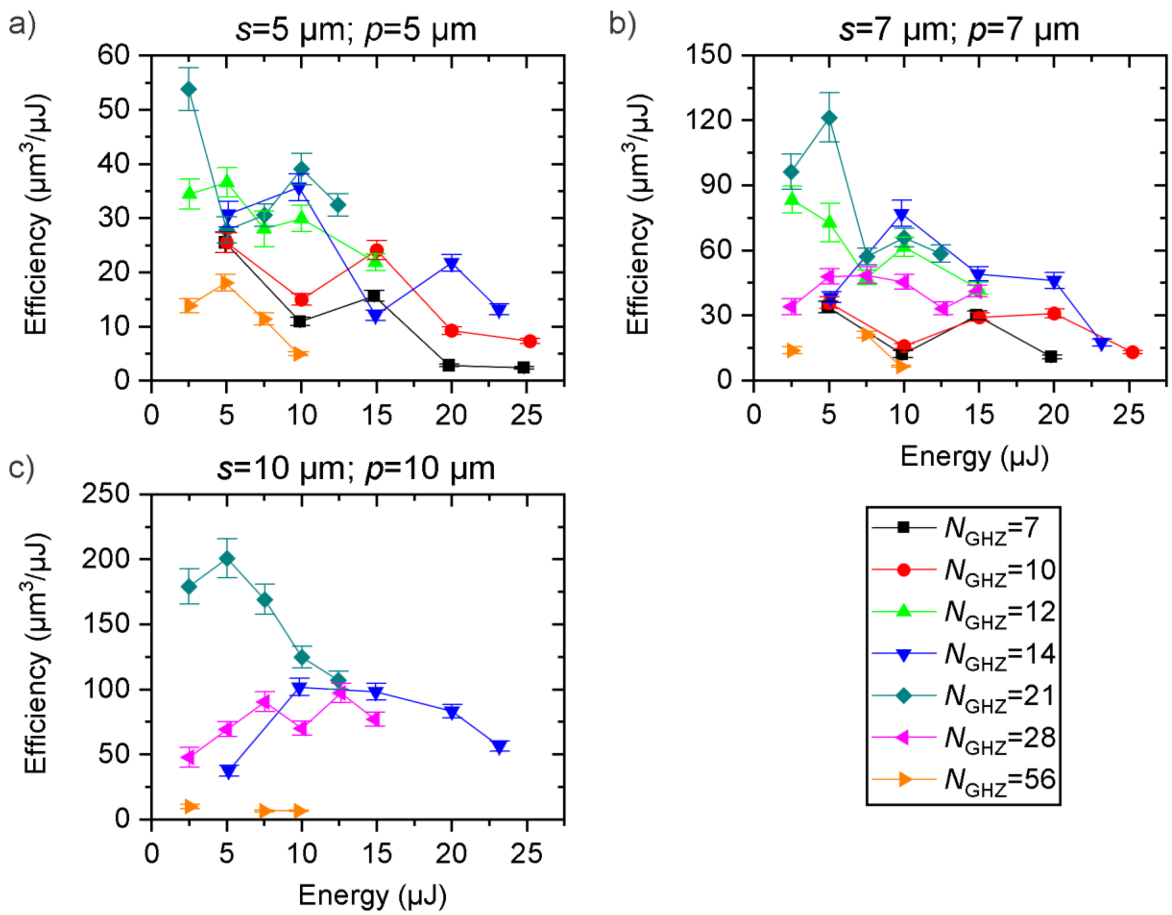

Figure 16. Milling efficiency dependence on energy when milling cavities with different spacing equal to pitch values of a) 5 µm, b) 7 µm, and c) 10 µm. N_{GHz} = 7; 10; 12; 14; 21; 28; 56. Lines are for eye guidance. Error bars are uncertainty.

GHz burst forms

Figure 17 milling efficiency using GHz bursts with different forms compared to the flat burst. Positive or negative form parameter indicates rising or falling energy of sub-pulses within the burst, respectively, and denotes the shape steepness.

Milling efficiency decreased when GHz burst form was changed to the non-flat burst form. Burst form parameter influence on burst temporal intensity was discussed in experimental setup section. Most of the pulses lost too much energy to contribute to milling. This effect was more pronounced with falling (negative) burst form. Therefore, milling with non-flat burst form resembled femtosecond milling, in terms of efficiency and quality.

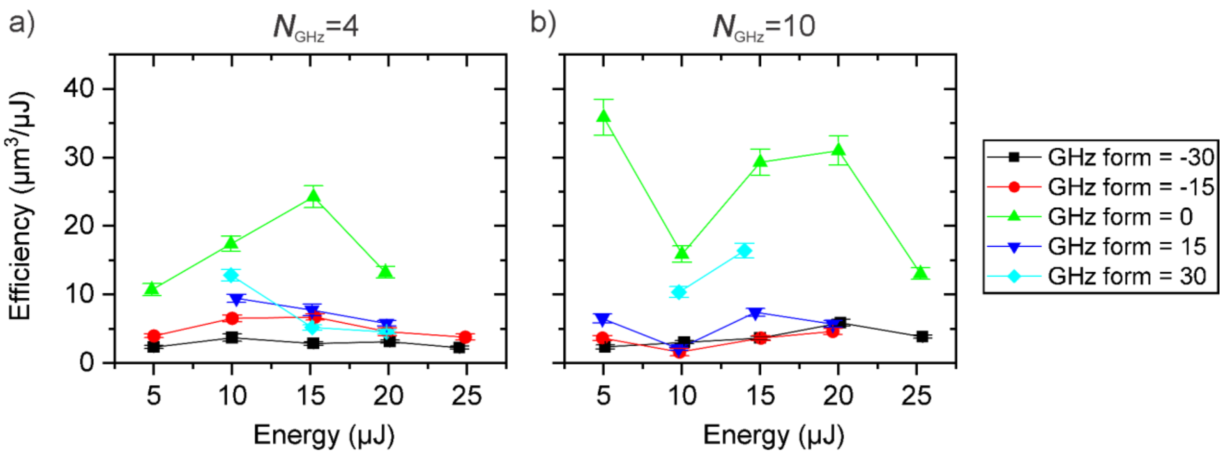

Figure 17. Milling efficiency dependence on energy when milling cavities with a) $N_{GHz} = 4$ and b) $N_{GHz} = 10$. Lines are for eye guidance. Error bars are uncertainty.

MHz and GHz burst regimes

Figure 18 shows milling efficiency using burst in a burst regime. We can see that in most cases higher efficiency was achieved when spacing and pitch was 5 µm. Increasing GHz pulse number did not show a clear dependence. The highest efficiency of 20.3±1.4 µm^3/µJ was achieved with $N_{MHz} = 2$ and $N_{GHz} = 5$, $E_b = 5$ µJ, $s = 5$ µm, $p = 5$ µm, $d_z = 5$ µm. Maximum milling efficiency was ~1.2 times lower than just with $N_{GHz} = 4$.

Milling efficiency with 2 µm spacing and 7 µm pitch changed little with different number of pulses in the GHz burst. There is a trend of decreasing efficiency with higher burst energy. Chipping was minimal <5 µm on average.

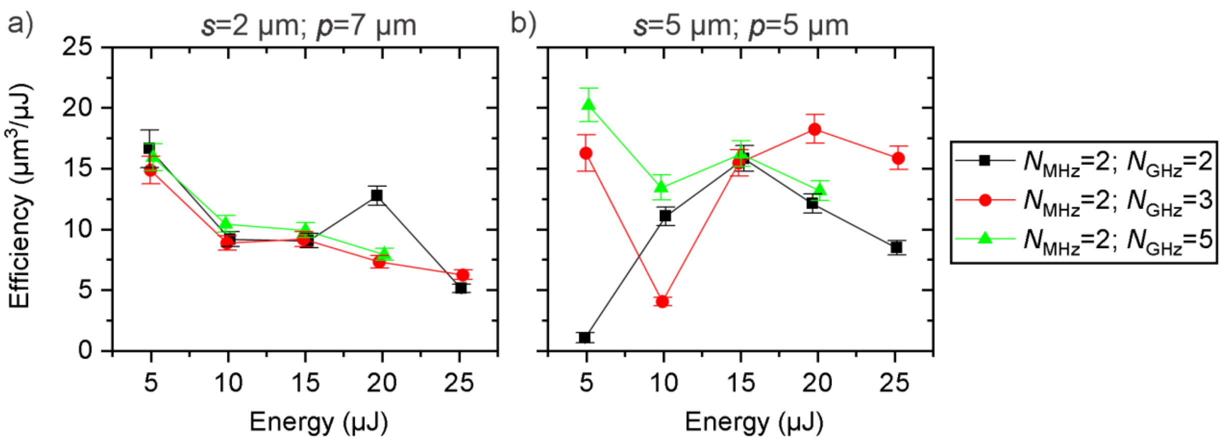

Figure 18. Milling efficiency dependence on energy when milling cavities with $N_{MHz} = 2$, different number of pulses in GHz burst, a) 2 µm spacing and 7 µm pitch, and b) 5 µm spacing and 5 µm pitch. Lines are for eye guidance. Error bars are uncertainty.

5.4. Milling rates using various bursts regimes

GHz burst regimes

Linear milling rate and material removal rate are plotted separately, because cavity diameter depends on spacing, pitch, d_z, and burst energy. Therefore, it is different for each data point resulting in different dependences between linear milling rate and material removal rate.

From Figure 19 we can see that the highest milling rate increases with higher number of pulses in the burst for $N_{GHz} = 2 – 4$. Milling rates were increasing for most regimes with higher burst energy up to ~15 µJ. With higher burst energies, milling rates decreased. In this N_{GHz} range, the highest linear milling rate of 0.66±0.03 mm/s was with $N_{GHz} = 4$, $E_b = 15$ µJ, $s = 5$ µm, $p = 5$ µm, and $d_z = 15$ µm. Material removal rate with the same parameter set was 0.31±0.01 mm^3/min.

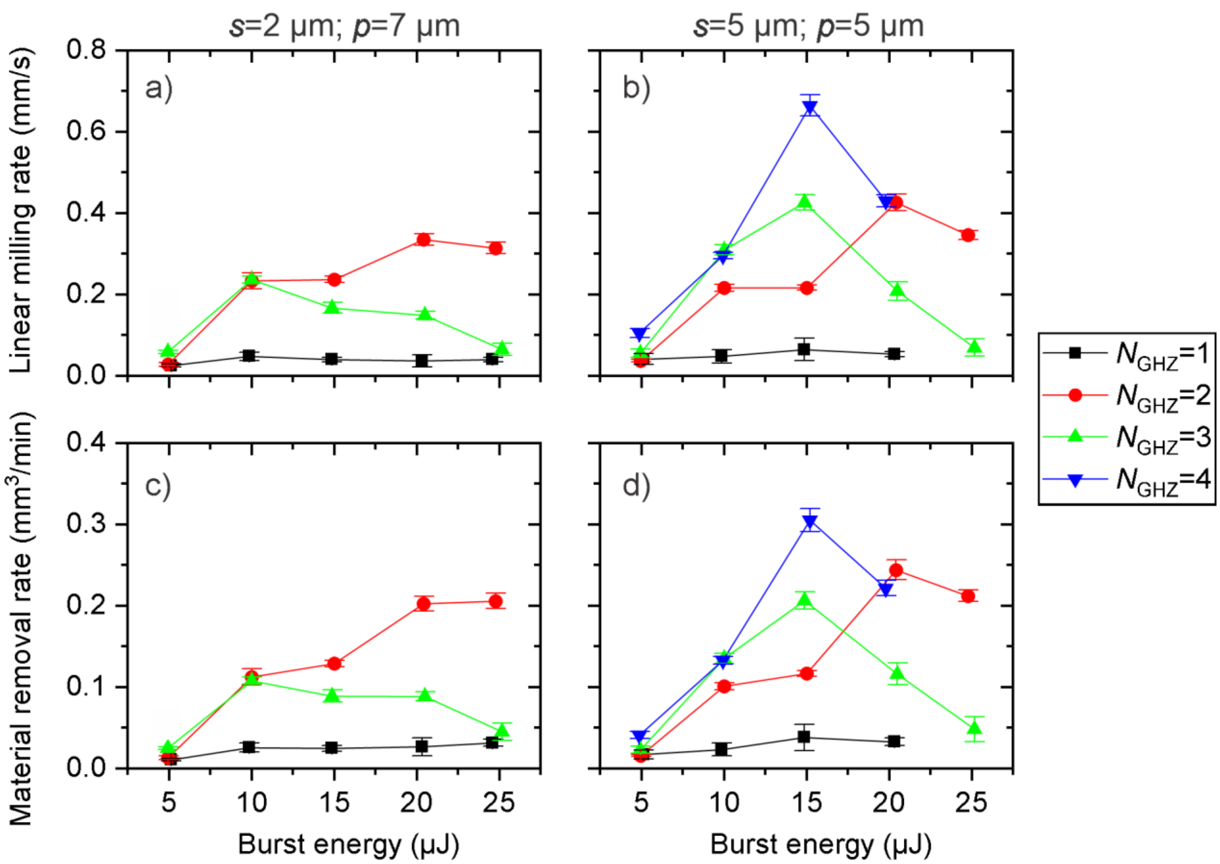

Figure 19. Linear milling rate and material removal rate dependence on energy when milling cavities with $N_{\mathrm{GHz}} = 1 – 4$ and a,c) 2 µm spacing, 7 µm pitch, and b,d) 5 µm spacing, 5 µm pitch. Lines are for eye guidance. Error bars are uncertainty.

Milling rate increased with higher spacing and pitch values. Figure 20 shows that as the number of pulses in the burst increased up to 21, milling rate increased. With and above $N_{\mathrm{GHz}} = 28$ milling rates started to decrease, except for few milling parameters. This decrease could be because of long interaction time which reached ~10 ns. From $N_{\mathrm{GHz}} = 56$ burst form is no longer flat-top which likely negatively influenced milling. At this regime, burst duration is ~20 ns.

The highest linear milling rate of 1.4±0.1 mm/s was achieved with $N_{\mathrm{GHz}} = 21$, $E_b = 7.5$ µJ, $s = 10$ µm, $p = 10$ µm, and $d_z = 15$ µm. In this case, material removal rate was 0.58±0.03 mm^3/min. However, around 1.4 times higher material removal rate was achieved with $N_{\mathrm{GHz}} = 14$.

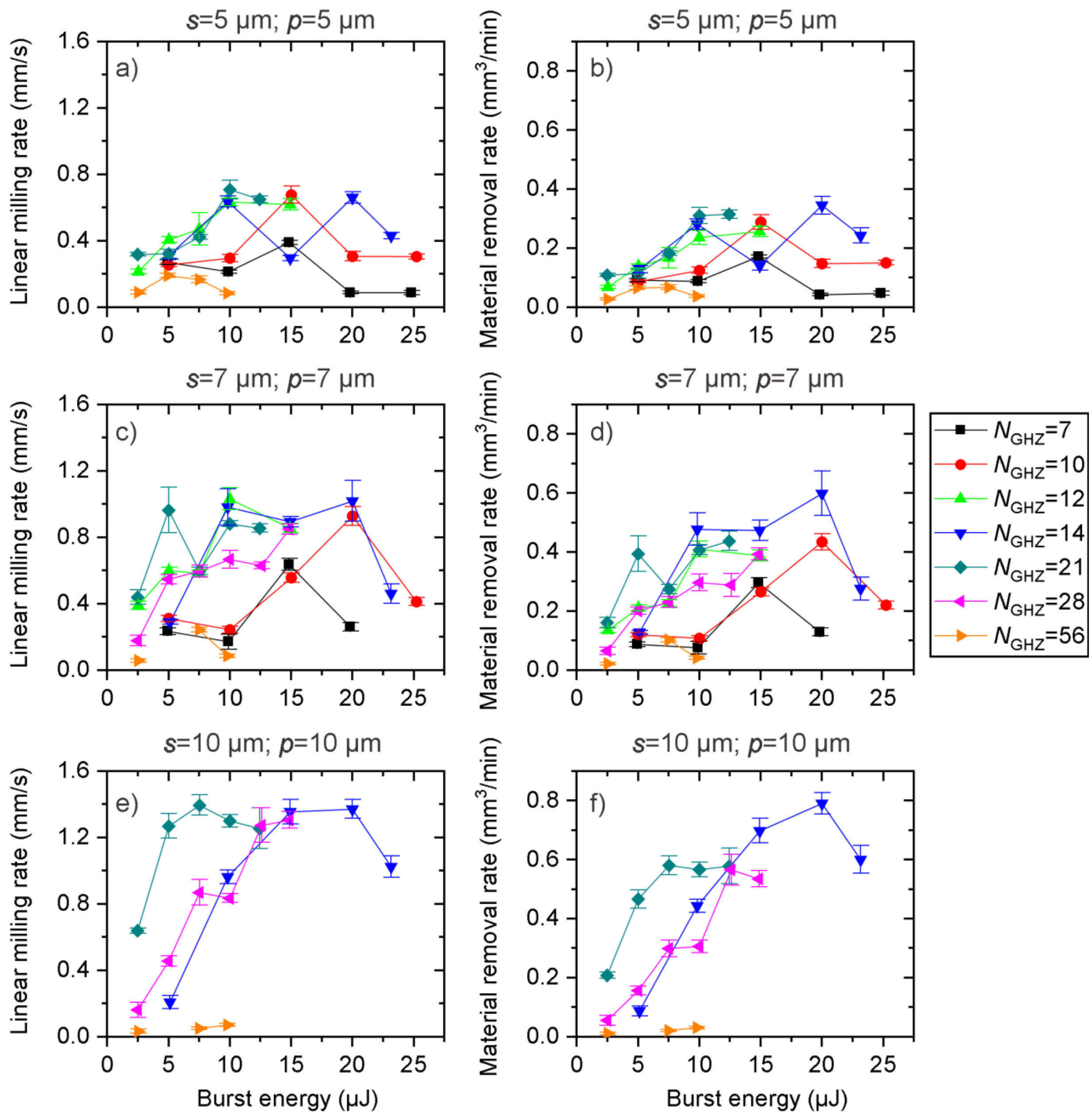

Figure 20. Linear milling rate and material removal rate dependence on energy when milling cavities with different spacing equal to pitch values of a,b) 5 µm, c,d) 7 µm, and e,f) 10 µm. N_{GHz} = 7; 10; 12; 14; 21; 28; 56. Lines are for eye guidance. Error bars are uncertainty.

GHz burst forms

As was mentioned in milling efficiency section, burst forms were likely too steep. This resulted in decreased milling rates for all forms when using $N_{GHz} = 4$, 10 (Figure 21).

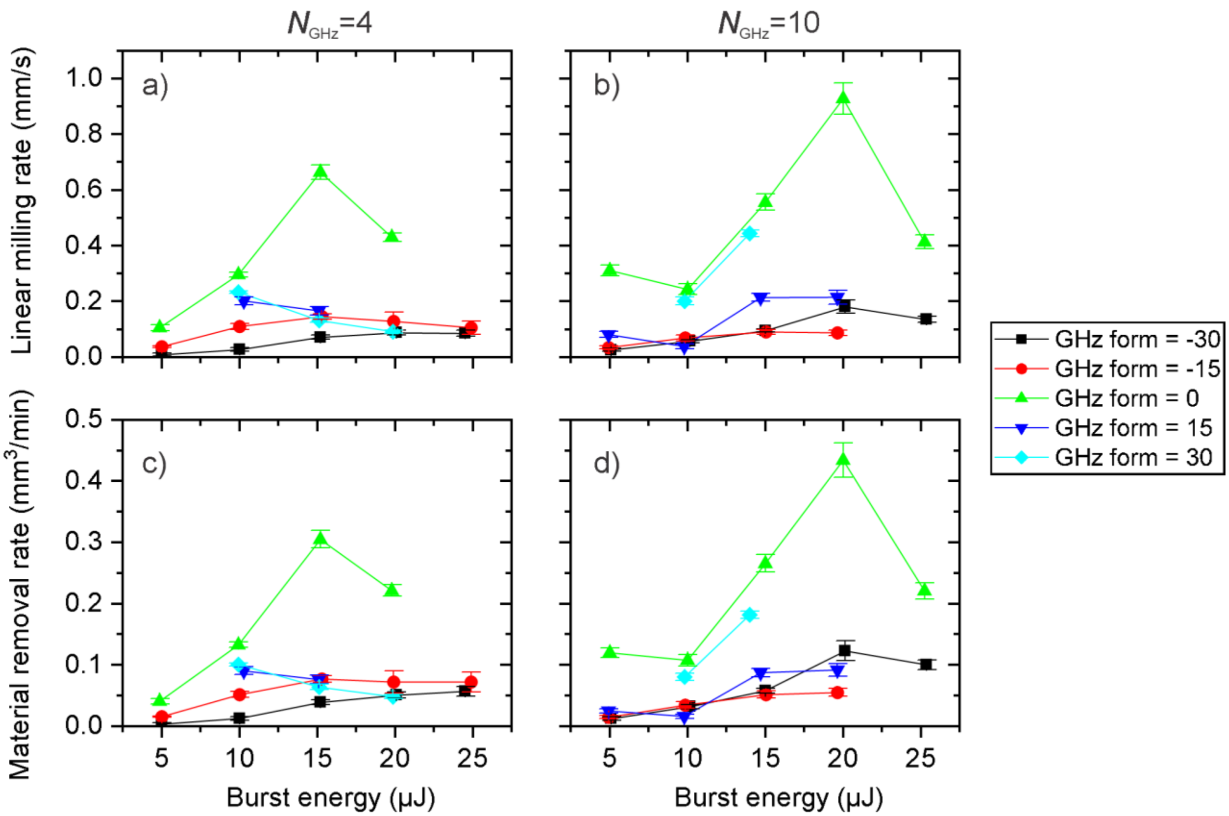

Figure 21. Linear milling rate and material removal rate dependence on burst energy when milling cavities with a,c) $N_{GHz} = 4$ and b,d) $N_{GHz} = 10$. Lines are for eye guidance. Error bars are uncertainty.

MHz and GHz burst regimes

When using both MHz and GHz burst regimes, highest milling rate with $N_{MHz} = 2$ and $N_{GHz} = 3$ was around 50% higher than with $N_{MHz} = 2$ and $N_{GHz} = 2$ or 5 (Figure 22). There was a trend of increasing milling rate with higher burst energies. However, linear milling rate and material removal rate were lower than just with $N_{GHz} = 4$.

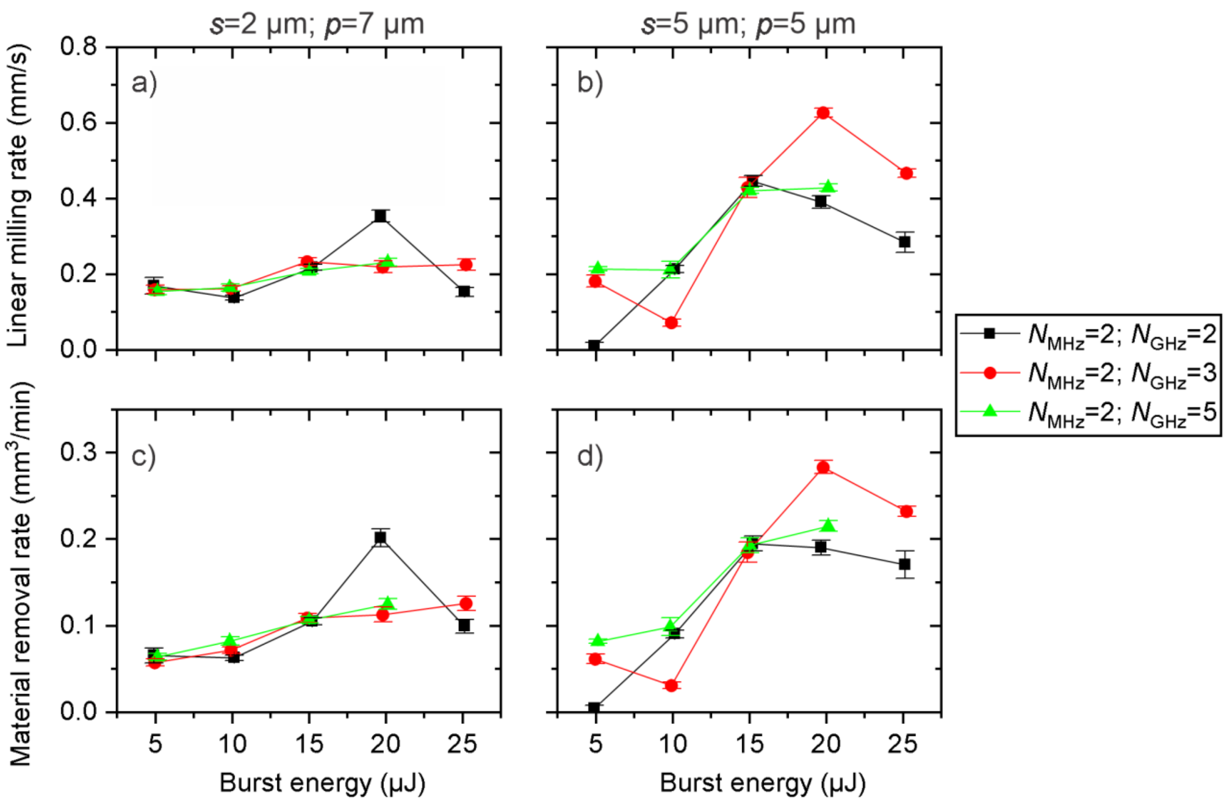

Figure 22. Linear milling rate and material removal rate dependence on energy when milling cavities with $N_{\mathrm{MHz}} = 2$, different number of pulses in GHz burst, a,c) 2 µm spacing and 7 µm pitch, and b,d) 5 µm spacing and 5 µm pitch. Lines are for eye guidance. Error bars are uncertainty.

5.5. Milling with nanosecond pulses

Milling efficiency increased with higher spacing and pitch values (Figure 23). There was a trend of decreasing efficiency with higher pulse energies for most parameter sets, however, the decrease was only around 40% for 4 ns pulses. Milling with 4 ns and 11 ns pulses resulted in similar milling efficiency and rate values. Higher pulse duration shifted the minimum pulse energy towards higher value (Figure 23 and Figure 24). This is because intensity is inversely proportional to pulse duration.

The highest efficiency of ~140±10 µm^3/µJ was when milling with s = 15 µm, p = 15 µm, d_z = 7 – 10 µm, E_b = 15–20 µJ, and 4 ns and d_z = 15 µm, E_b = 30 µJ, and 11 ns (Figure 23).

The highest linear milling rate was ~1.5±0.1 mm/s with E_b = 30 µJ, s = 15 µm, p = 15 µm, and d_z = 15 µm for both 4 ns and 11 ns pulse durations (with 11 ns SD was two times larger). Material removal rate at the same parameter set was 0.69±0.05 mm^3/min.

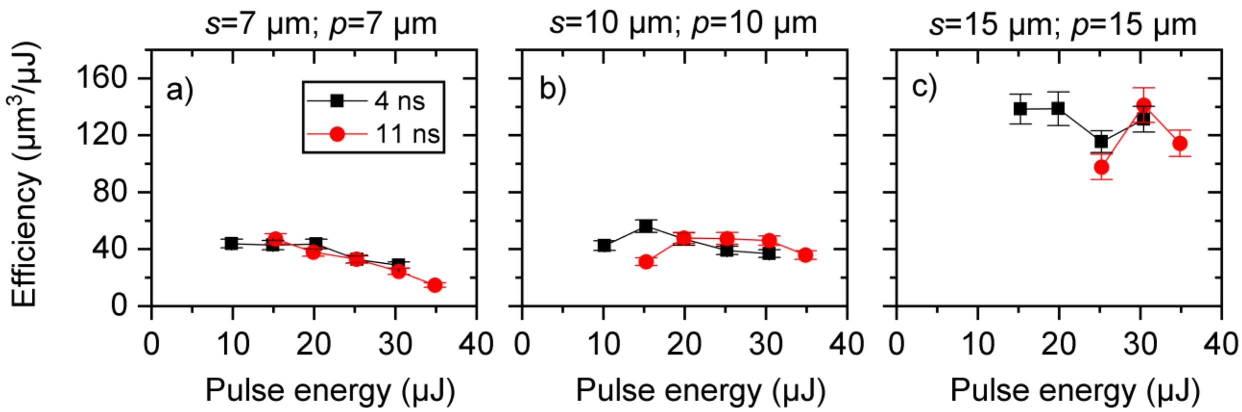

Figure 23. Milling efficiency dependence on pulse energy when milling cavities with 4 ns and 11 ns pulses with different spacing equal to pitch values of a) 7 µm, b) 10 µm, and c) 15 µm. Lines are for eye guidance. Error bars are uncertainty.

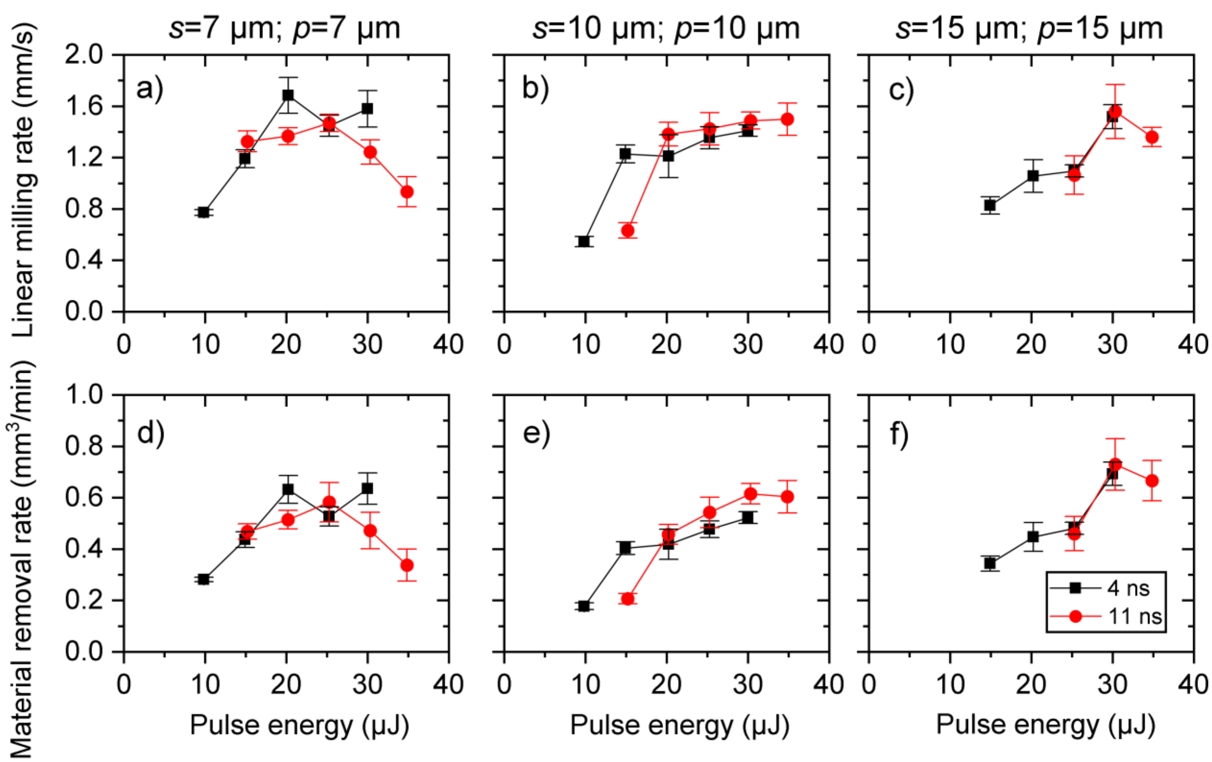

Figure 24. Linear milling rate and material removal rate dependence on pulse energy when milling cavities with 4 ns and 11 ns pulses with different spacing equal to pitch values of a,d) 7 µm, b,e) 10 µm, and c,f) 15 µm. Lines are for eye guidance. Error bars are uncertainty.

5.6. Airflow optimisation

It was impossible to mill through glass vias in 6.3 mm thickness fused silica with the same parameters as used in cavity milling above. $N_{GHz} = 4$, $E_b = 15$ µJ, $s = 5$ µm, $p = 7$ µm, and $d_z = 5$ µm parameter set was acquired after optimising for the highest milling rate with the lowest possible number of pulses in a burst. Using this parameter set, the largest cavity depth of 1 mm was achieved.

5 cavities were milled with 0.5 mm centre-to-centre distance. Nozzle centre was positioned below the middle cavity. This resulted in larger milled depth for the middle cavity compared to nearby cavities. Milling loops were changed by 25 giving ~90 µm step error which is shown as error in Figure 25. The highest milled depth of 8.5 mm was achieved with de Level nozzle at 25 mm distance between nozzle tip and the bottom of a sample. All other nozzles had minimal impact on cavity depth, except conical spray nozzle. Milled depth steadily increased up to ~3 mm with lower sample-to-nozzle distance when using conical spray nozzle.

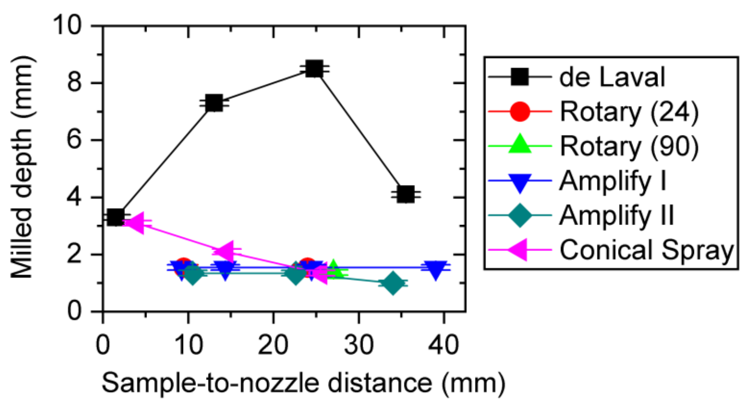

Figure 25. Milled depth dependence on sample-to-nozzle distance when using different nozzles. Airflow pressure was 0.8 MPa. Lines are for eye guidance. Error bars are ~90 µm step error.

5.7. TGV matrix milling

Airflow from a de Laval nozzle was required to achieve higher depth cavities as discussed above. The nozzle exit was 16 mm below the sample and 0.8 MPa air was blown at the milling area. This resulted in through glass vias in 6.3 mm fused silica. Precise centering of milling area in respect to the nozzle position was needed to achieve the best results. Over ~1 mm translation from centre led to worse quality cavities or cracking, while central cavities were successfully and repeatably milled.

When milling TGV matrices, the minimal centre-to-centre distance can be calculated from $p_{min} = d + h*\tan(\theta_m)$. Here, θ is the angle of incident laser beam ($\theta = 0.14$ rad), θ_m is refracted beam angle, d is the diameter of the TGV ($d \approx 0.1$ mm), and h is the thickness of fused silica sample. The minimal distance is around 700 µm for 6.3 mm thickness samples. Figure 26 a) shows how beam scattering limits the minimal distance between nearby channels. Figure 26 b) shows segmented milling technique, where only a part of the channel depth is milled for all channels. After that milling is repeated, increasing the depth by multiple segments. This results in nearby channels not being deep enough to scatter laser light.

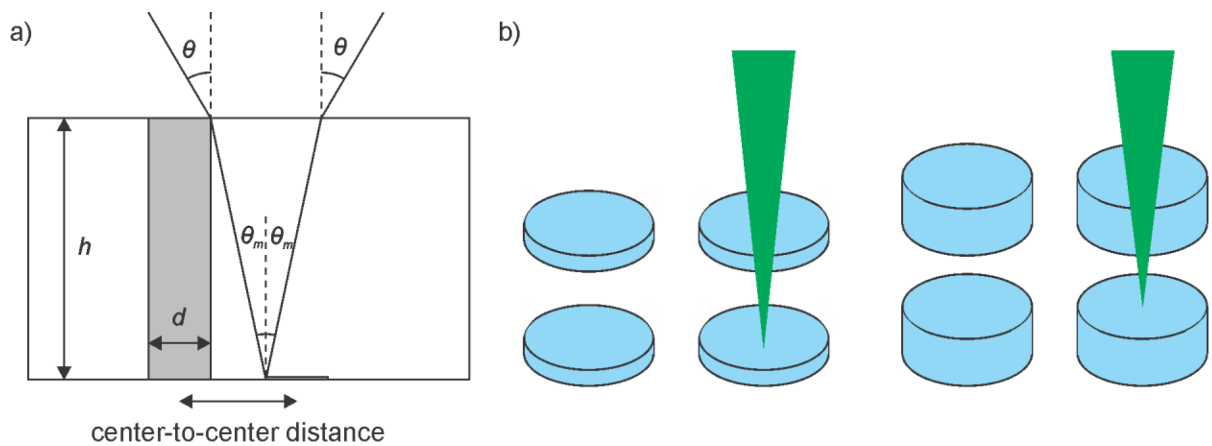

Figure 26. Scheme for a) milling TGVs next to each other and b) segmented milling.

Figure 27 shows how lower number of pulses in a GHz burst resulted in better quality in terms of chipping, however, there was more debris stuck to the channel walls. Milling parameters with calculated milling efficiency and rate are shown in Table 3. Higher GHz count resulted in around 2 times faster and more efficient milling. However, chipping was ~40 µm on the top side and ~25 µm on the bottom side of the sample. Using $N_{GHz} = 4$, chipping was ~20 µm on the top side and ~10 µm on the bottom side of the sample.

It was possible to reduce the channel-to-channel distance to 300 µm. This distance is ~400 µm lower than theoretically calculated. Denser packing was likely achieved because of self-focusing which was not included in the theoretical calculation and because only a part of the beam is scattered which does not lead to immediate failure. Further channel-to-channel distance reduction resulted in channels with lower circularity after the first TGV or failure in terms of cracking. To mitigate this effect, cavities could be milled with a segmented milling. However, this approach would result in multiple times longer milling times (from previous results ~3 times longer).

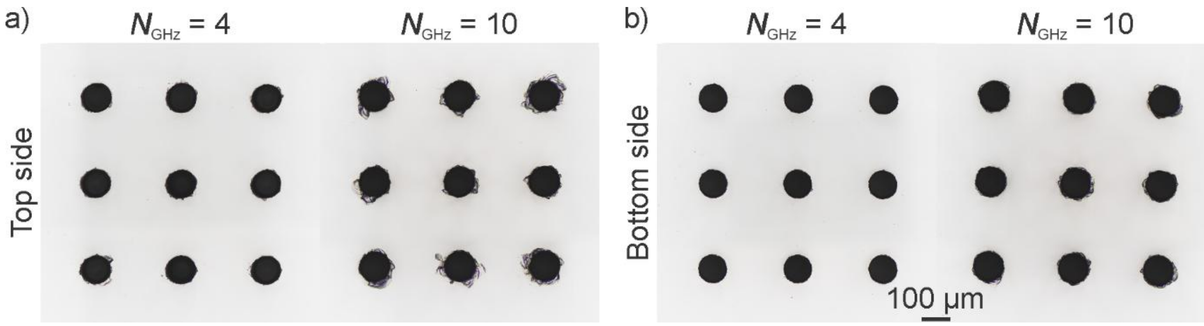

Figure 27. Microscope pictures of a) top side and b) bottom side of TGVs in 6.3 mm fused silica with N_{GHz} = 4 and 10. Channel-to-channel distance was 300 µm.

Table 3. Airflow assisted milling parameters for high quality and fast drilling.

N_{GHz}	E_b, µJ	s, µm	p, µm	d_z, µm	N_l	t, s	η, µm^3/µJ	v_l, µm/s
4	10	5	7	5	950	28.7	10.7	221
10	20	7	7	10	490	12.5	19.1	505

Additionally, through glass vias were milled in 1 mm thickness fused silica. Airflow was not used because ~1 mm depth can be milled without it and to avoid sample breaking. Milling was divided into segments of 10 loops. Thus, resulting in the reduction of channel-to-channel distance to 110 µm (Figure 28). Without segmentation, milling is less repeatable, likely due to top surface chipping blocking and scattering the laser beam for nearby channels.

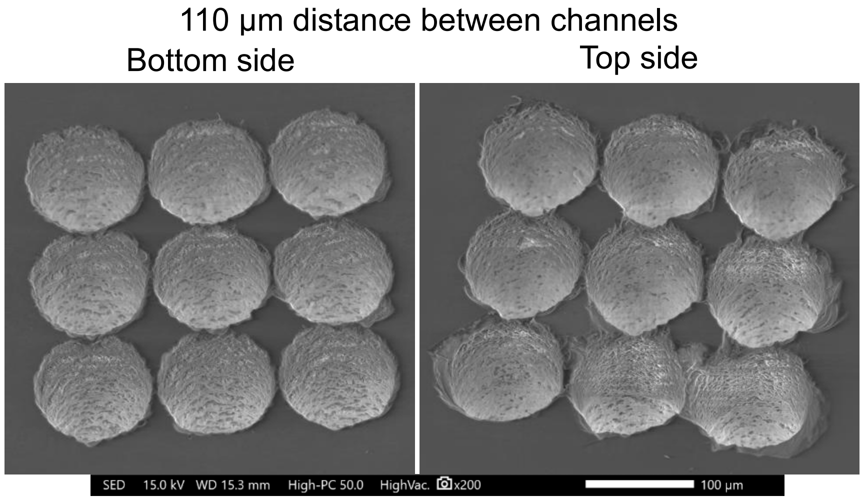

Figure 28. Scanning electron microscope (SEM) images of TGVs milled in 1 mm thickness fused silica. Segmented milling with $N_{GHz} = 7$.

5.8. Quality investigation of TGV

5 channels with 300 µm distance between them were milled in 6.3 mm FS and characterized. Mean values and standard deviation of roughness parameters and maximum chipping was estimated. Milling parameters are shown in Table 4. Nozzle airflow pressure was 0.8 MPa and it was positioned 26 mm below the sample. It was not possible to retain the same parameter set for all burst regimes. For burst counts of 7 and higher, it was sufficient to increase just the burst energy to 15 µJ.

Table 4. TGV milling parameters.

N_{GHz}	E_b, µJ	Pitch, µm	Spacing, µm	d_z, µm	Loops	Milling time, s
4-6	10	7	5	5	970	29.5
7-10	15	7	5	5	970	29.5

Measurement of broken sample was difficult because sample broke in chaotic non-uniform manner. This resulted in some channel not opening fully and required to zig zag a line across the topography to achieve the required evaluation length (5.6 mm) for ISO 25178 standard. Additionally, samples were prepared where TGVs were milled with an offset from the breaking line and then polished until the channels were opened. Roughness measurements are shown in Figure 29. In most cases, the roughness of polished and as cleaved samples was comparable (with overlapped standard deviations). There was a tendency of increasing roughness with higher burst count. The profile roughness parameters Ra and Rz were below 1.4 µm and 16 µm, respectively, for the burst regime with the lowest count.

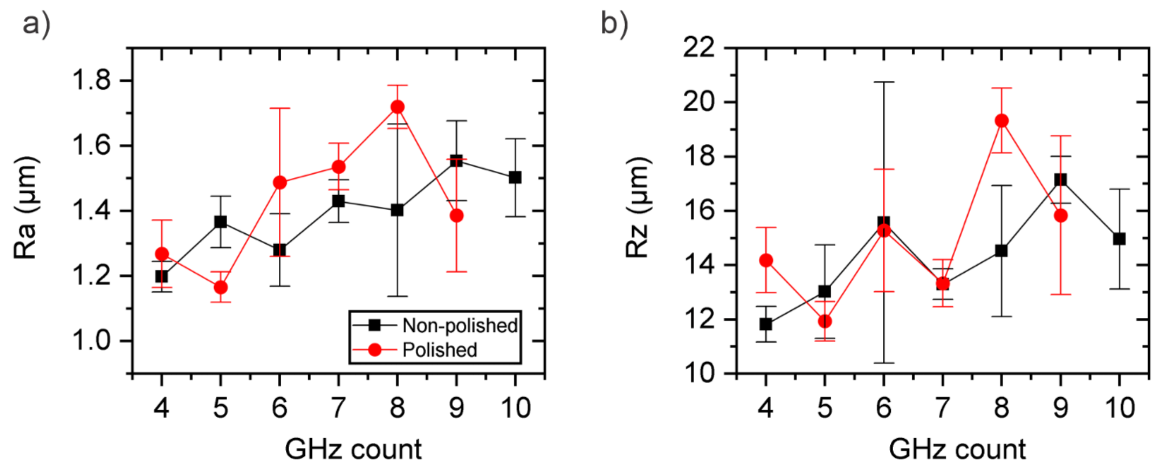

Figure 29. Sidewall profile roughness a) Ra and b) Rz dependence on number of pulses in GHz burst. Samples were measured when TGVs were milled colinearly with the breaking line and with some offset and then mechanically polished. Error bars indicate standard deviation. Lines are for eye guidance. Error bars are standard deviation.

The length of chipping was measured for each cavity in investigated parameter set, measured from the cavity opening to the longest chip collinearly to cavity radius. Due to random nature of chipping and because the milling parameters were not optimized for each burst regime, chipping appears to be decreasing with higher number of pulses in the burst on the top side of the sample (Figure 30). This reduction could come from reduced individual pulse intensity with higher bursts, which reduces top-down ablation near the end of milling. Furthermore, with a small number of pulses in the burst (<7) there is a large standard deviation. On the contrary, chipping on the bottom side was increasing. Channels with the largest chipping were shown in Figure 31. With higher number of pulses in the burst chipping takes up a larger arc of the channel and is deeper (appears darker).

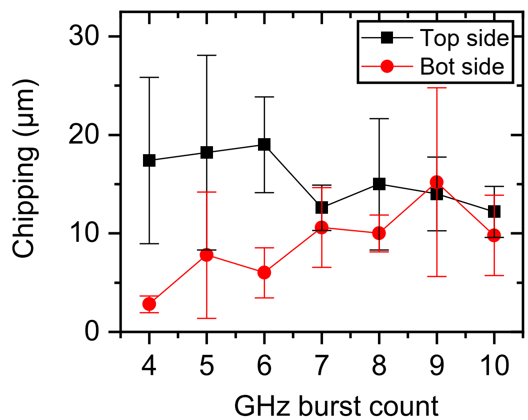

Figure 30. Chipping dependence on GHz burst count. Lines are for eye guidance. Error bars are standard deviation.

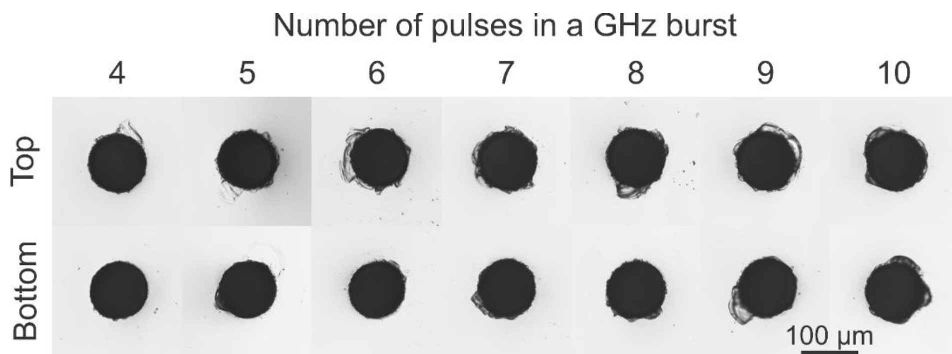

Figure 31. Microscope images of top and bottom sides of TGVs.

From Figure 32 a) it is seen that chipping on the top side of the sample increases with increasing vertical step d_z, while bottom side chipping remains the same within standard deviation. From Figure 32 b) it is seen that with $N_{GHz} = 10$ all chipping values were within standard deviation showing no clear dependence. Increasing burst energy by 2.5 µJ for $N_{GHz} = 4$ and 10 µJ for $N_{GHz} = 10$ results in minor increase in chipping on the bottom side of the sample while top side is within standard deviation.

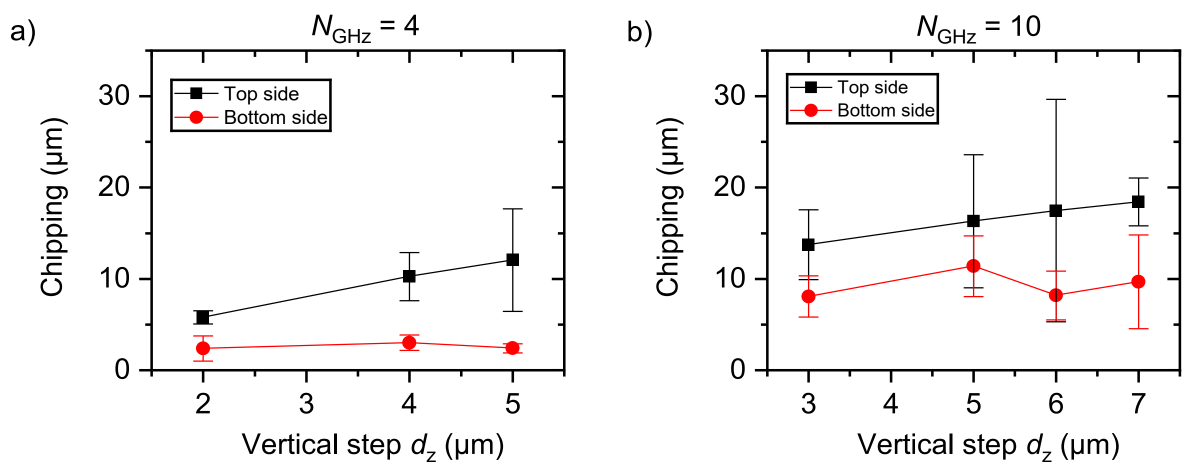

Figure 32. Chipping dependence on laser milling parameters for a) $N_{GHz} = 4$ and b) $N_{GHz} = 10$. Lines are for eye guidance. Lines are for eye guidance. Error bars are standard deviation.

5.9. TGV metallisation

TGV channels were milled in indented sample as described in method section (Figure 12). TGV milling parameters were $N_{GHz} = 4$, $E_b = 10$ µJ, $s = 5$ µm, $p = 7$ µm, $d_z = 5$ µm, and $N_l = 970$. Five vias were drilled with the same parameter set. Metallisation parameters were different for samples on left and right sides in Figure 33. Metallisation was done with selective surface activation induced by laser (SSAIL) technique [1, 35, 36] in 3D Technologies and Robotics Laboratory (FTMC). Surfaces are modified by a laser. These areas have selective adhesion to catalysis activation process where solution with metal particles adheres to the surface. Final process of copper deposition happens only the activated areas [35, 36].

Sample breaking was non-uniform when TGVs were milled collinearly with the breaking line as seen in Figure 33 a). This made it difficult to measure how much depth got metallised. Additional samples were prepared with channels milled around 300 µm away from the breaking line. After breaking the sample, they were mechanically polished until the channels were open. Samples were cleaned in an ultrasonic bath for 30 min in acetone before taking microscope pictures of top and bottom side of TGVs. After polishing they were cleaned again for 15 min to remove the wax-like material holding them to the polishing plate and 15 min again in clean acetone to fully remove polishing slurry and other debris. From the polished sample (Figure 33 b) we can see that metallisation reached about 2 mm depth on both sides of the TGV. Metallisation in Figure 33 b) resulted in TGVs with closed top and bottom entrances, while a) were see through.

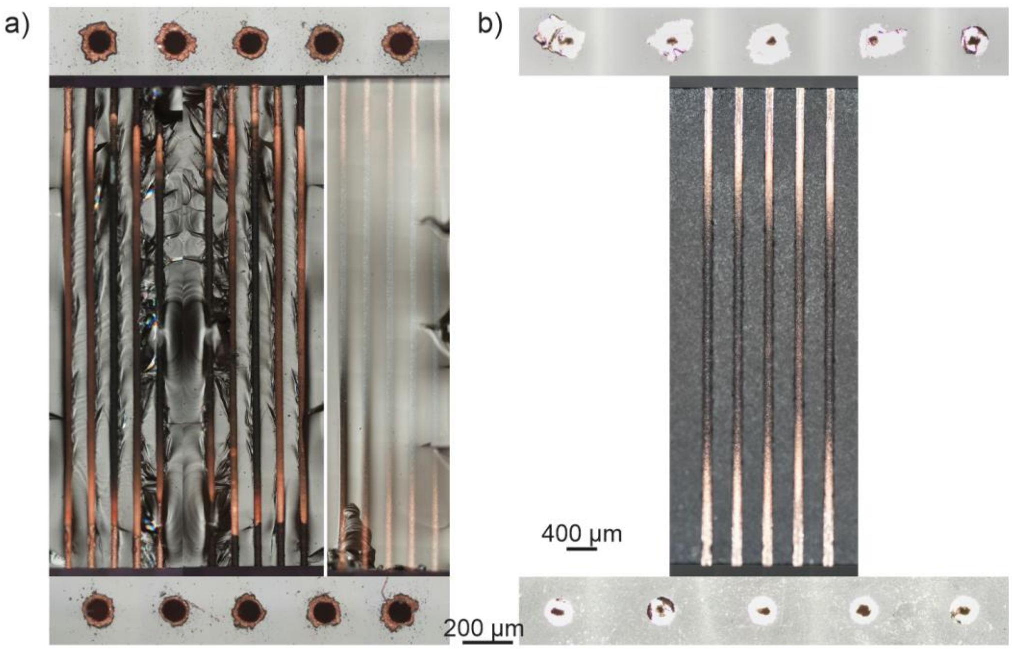

Figure 33. Microscope images of metallised TGVs when a) TGVs were milled collinearly with the breaking line and b) TGVs were milled with an offset to the breaking line. 400 μm scale is for broken sample images, 200 μm scale is for top and bottom side of TGVs. Top side of the images corresponds to top side of milling.

5.10. Complex shape fabrication

Complex shape consisted of a 100 μm-diameter hole in 6.3 mm-thick glass with 1 mm-depth and radius fillets on both sides. This is a challenging task requiring both, bottom-up and top-down processing techniques. For optimization of top-down milling, cavities with 1 mm radius were milled at different fluence values. Milling efficiency dependence on fluence is shown in Figure 34 for different spacing and pitch values for non-burst regime and $N_{\mathrm{GHz}} = 4$. The best results were achieved with fluence below 12 J/cm^2 for spacing and pitch values above 1 μm. As fluence increased, milled surface topology became concave and volumetric chipping started to develop at the contour.

Further milling was done using femtosecond laser burst regime with the same number of pulses in as with high-quality TGV milling ($N_{\mathrm{GHz}} = 4$). We can see that increase in efficiency was almost twofold with the burst regime reaching 9.3 μm^3/μJ. Additionally, chipping was still relatively small, up to ~7 µm. Therefore, it was possible to utilise the same GHz burst regime throughout the hole milling, which speeds ups processing by a few minutes which are needed for the laser power to stabilise after switching burst modes.

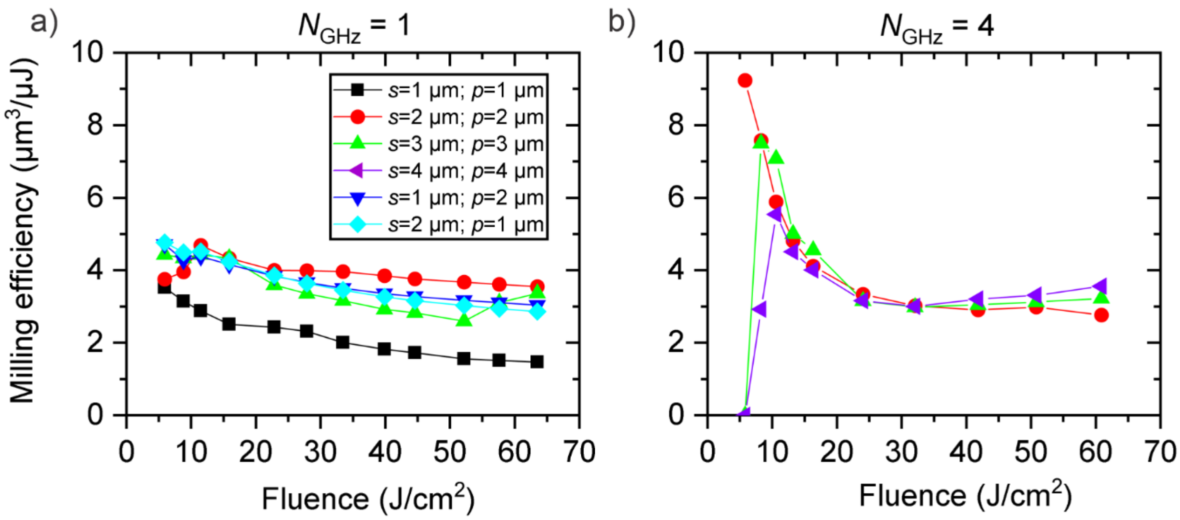

Figure 34. Milling efficiency dependence on fluence for different spacing and pitch values when milling a) without burst and b) with $N_{GHz} = 4$. Lines are for eye guidance.

TGV with round top and bottom

Milling round bottom with the same parameters as TGV resulted in poor initiation and therefore the round form was incorrect. An initiation step was added to damage the bottom surface. However, milling after the initiation still resulted in poor milling or cracking of round form with large diameters. Therefore, after initiation, around 15 µm depth was milled to make the surface homogenous. Initiation on the top side was simpler and only a single loop was used to damage the surface before milling the round shape.

Round shape form was calculated from a circle equation (15-18). Here Δh is the change in height, Δr is the change in radius, R is curvature radius, d is current depth, r_c is current channel radius. Additionally, d was multiplied by refractive index for round bottom milling.

$$\Delta h^2 + \Delta r^2 = R^2. \tag{15}$$

$$\Delta h = R - d. \tag{16}$$

$$r_c = R - \Delta r. \tag{17}$$

$$r_c = r_0 + R - \sqrt{2Rd - d^2}. \quad (18)$$

A TGV with 1 mm radius curvature entrance and exit was milled (Figure 35). Milling parameters of each step are given in a chronological order in Table 5. Topographies were measured using confocal profilometer (Sensofar S neox). Curvatures were measured using the sensoVIEW software and ranged from ~915 µm to ~1010 µm.

Table 5. TGV drilling with round entrance and exit parameters for each step.

Part	N_{GHz}	E_b, µJ	p, µm	s, µm	d_z, µm	Offset, µm	Loops
Initiation bottom I	4	1	4	4	30	100	4
Initiation bottom II		10	5	5	5	270	5
Round bottom		10	5	5	2	230	339
TGV		10	7	5	5	0	900
Initiation top		2	2	2	0	0	1
Round top		2	3	3	1.5	0	660

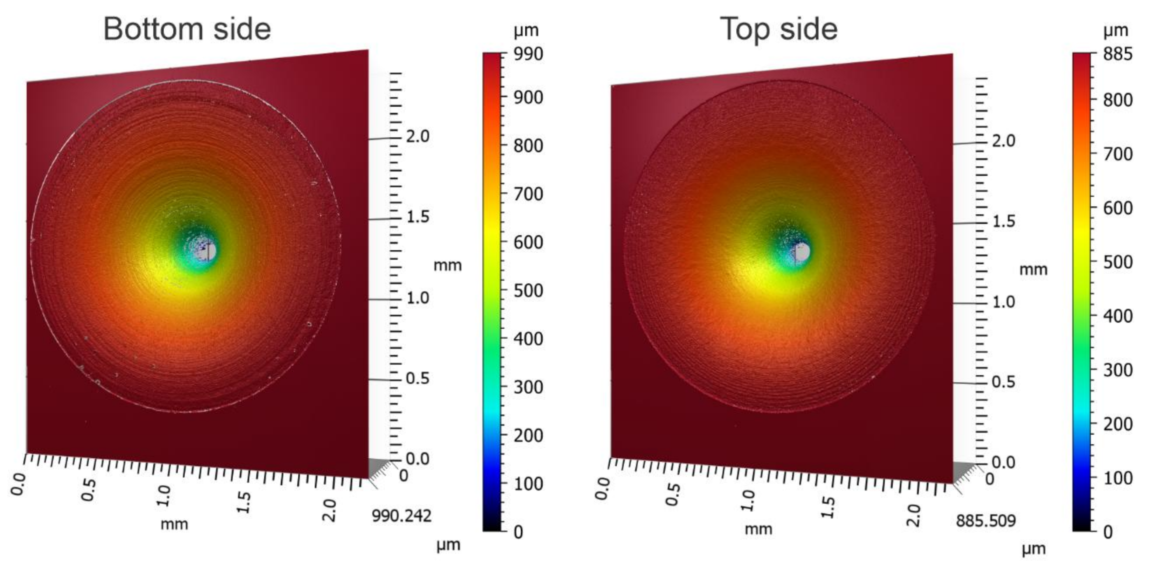

Figure 35. Topographies of bottom and top side of TGV with round entrance and exit.

6. Overview

TGV chipping was measured when milling with N_{GHz} = 4–10 and E_b = 10 or 15 µJ. Chipping increased with higher number of pulses in the burst at similar burst energies from <5 µm to ~15 µm on the bottom side. On the contrary, top side chipping decreased from ~20 µm to ~15 µm.

When milling blind holes, increase in burst energy in most cases resulted in larger chipping. For burst/pulse energy below 25 µJ chipping was around 20–25 µm for GHz burst and nanosecond pulses (Figure 36). At larger energies random and significantly larger (more than cavity radius) chipping appears which can be seen in Figure 37 with 11 ns pulses and N_{GHz} = 14 at their highest energies. Longer nanosecond pulses produced larger chipping at and above 25 µJ pulse energy. Changing spacing and pitch values did not significantly change the chipping values. From TGV milling quality disscused in section 5.7 we can see that, when N_{GHz} < 9 chipping on the bottom side is below 15 µm and decreases to below 5 µm with N_{GHz} = 4.

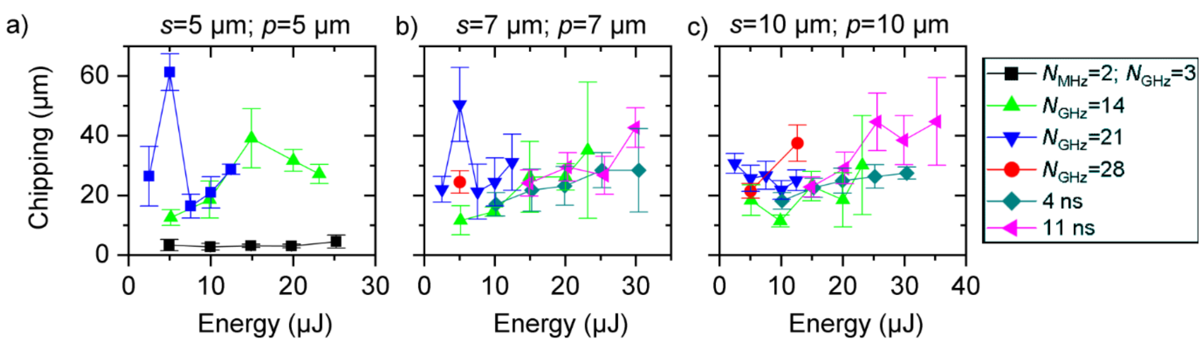

Figure 36. Chipping dependence on number of pulses in a GHz burst and chipping dependence on burst/pulse energy when milling with various bursts, ns pulses, and different spacing equal to pitch values of a) 5 µm, b) 7 µm, and c) 10 µm. Graphs with energy depict bottom side chipping. Lines are for eye guidance. Error bars are standard deviation.

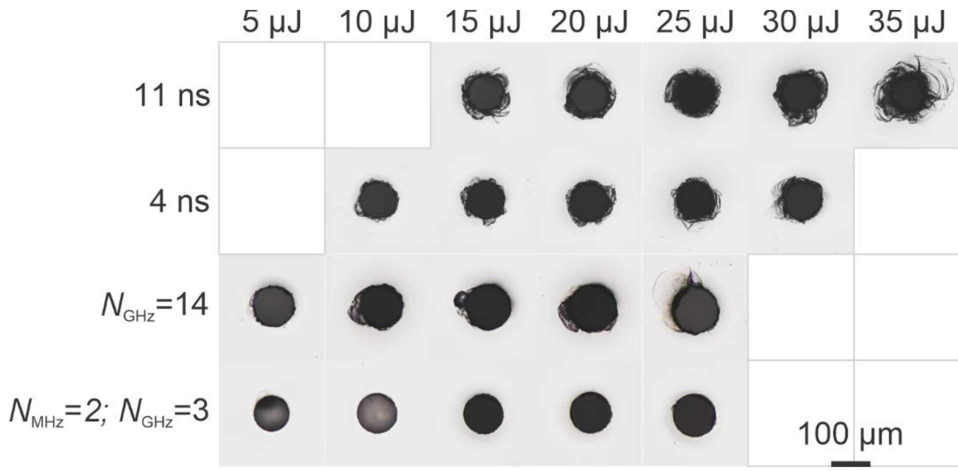

Figure 37. Microscope images of cavities milled with nanosecond (4 and 11 ns) pulses and with burst regimes of N_{GHz} = 14 and N_{MHz} = 2, N_{GHz} = 3.

The time difference between GHz pulses is ~360 ps, which means that 4 and 11 ns pulses would be equivalent to around N_{GHz} = 12 and 31, respectively (nanosecond pulses were plotted at these N_{GHz} in Figure 38 and Figure 39).

Milling efficiency with nanosecond pulses was more efficient than with GHz bursts near equivalent burst durations (Figure 38). However, the highest milling efficiency of 201±15 $\mu m^3/\mu J$ was achieved with N_{GHz} = 21 which was ~1.4 times higher than with nanosecond pulses.

From Figure 39 we can see that the highest linear milling rate of 1.5±0.1 mm/s was achieved with nanosecond pulses which was only ~1.1 times faster than with N_{GHz} = 14 or 21. While the highest material removal rate of 0.79±0.04 was with N_{GHz} = 14 only ~1.1 times faster than with nanosecond pulses.

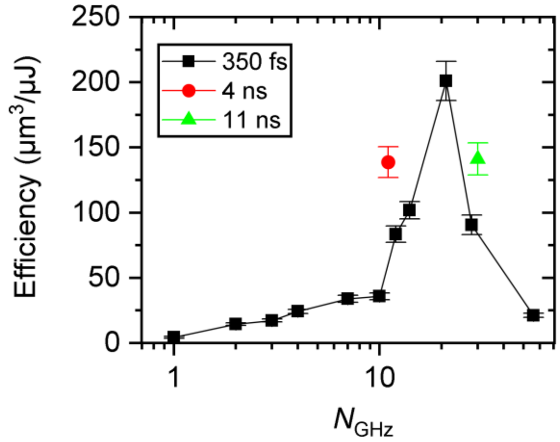

Figure 38. Milling efficiency dependence on the number of pulses in the burst. 4 ns and 11 ns pulses plotted by their equivalent number of pulses in GHz burst. Lines are for eye guidance. Error bars are uncertainty.

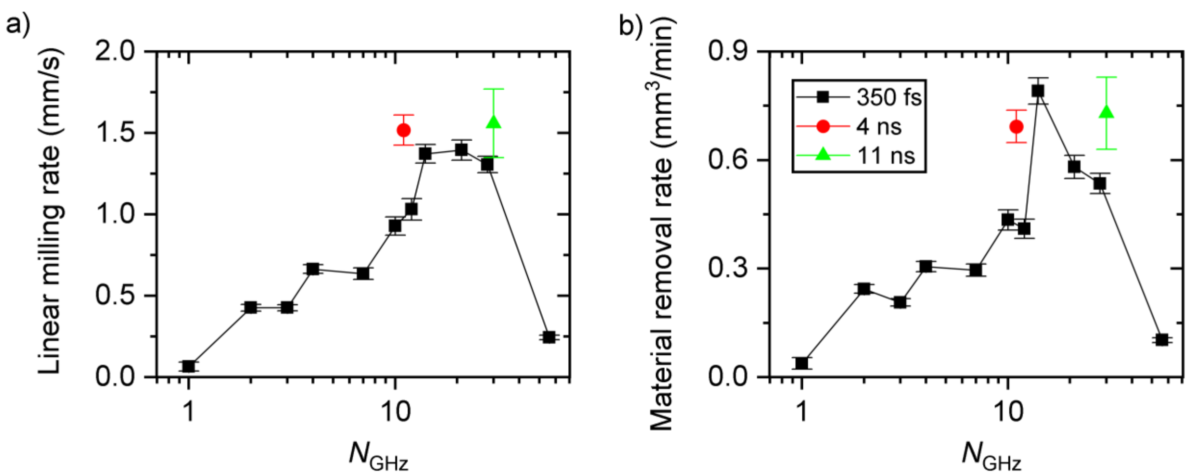

Figure 39. a) linear milling rate and b) material removal rate dependence on the number of pulses in the burst. 4 ns and 11 ns pulses plotted by their equivalent number of pulses in GHz burst. Lines are for eye guidance. Error bars are uncertainty.

Comparison to literature

All the literature sources compared in Table 6 are for milling fused silica. When using a GHz burst regime with 15 pulses in the burst, 12.7 times increase in milling efficiency compared to non-burst regimes was reported by L. Zubauskas *et al.* [20]. Milling area was 2×2 mm^2 in fused silica, 1030 nm wavelength laser with pulse duration of 176 fs was used. GHz burst repetition rate was 2.13 GHz, while MHz burst repetition rate was 63.3 MHz. Flat burst profile with the last pulse having 3 times larger intensity. In the same paper, they have also reported that using both the MHz and GHz regime together, burst in a burst or BiBurst, resulted in even larger increase in efficiency which was 24.3 times larger than without burst regime (N_{GHz} = 30 and N_{MHz} = 5). Similar milling efficiency was reported by S. Schwarz *et al.* [18] when milling with similar laser parameters (pulse duration, wavelength, burst repetition rate), but with N_{GHz} = 10. MHz regimes were reported to have lower milling efficiency than GHz burst regimes [37].

Table 6. Comparison of milling with burst regimes. In chipping column * represents bottom side.

Feature	Milling method	Burst/pulse	η, $\mu m^3/\mu J$	v_l, mm/s	Chipping, µm	Source
2×2 mm^2 square	Top-down	2.13 GHz *N*=15	49			[20]
1×1 mm^2 square	Top-down	2.17 GHz *N*=10	50.83			[18]
1×1 mm^2 square	Top-down	2.5 GHz *N*=5	27			[38]
(1.5-3.5)×0.3 mm^2	Top-down	60 MHz *N*=5	18.3			[37]
Ø 100 µm TGV	Bottom-up	4.5 ns laser	60		60/130*	[32]
Ø 100 µm blind-hole	Bottom-up	4 ns laser	140±10	1.5±0.1	~27*	This work
Ø 100 µm TGV	Bottom-up	2.8 GHz *N*=4	10.7	0.22	~20/10*	This work
Ø 100 µm TGV	Bottom-up	2.8 GHz *N*=10	19.1	0.51	~40/25*	This work
Ø 100 µm blind-hole	Bottom-up	2.8 GHz *N*=21	201±15	1.4±0.1	~25*	This work

7. Main results and conclusions

1. Low number of ultrashort laser pulses in a GHz burst (N_{GHz} = 4) enables high-quality bottom-up milling of small diameter (≈100 µm) through holes in fused silica with sidewall roughness Ra 1.2±0.1 µm and surface chipping below 25 µm using 515 nm wavelength.
2. Transition to more apparent glass fracturing at higher number of pulses in a GHz burst results in more clean and efficient milling, reaching 201±15 $\mu m^3/\mu J$ at 21 pulses per burst; however, accompanied by increased surface chipping.
3. Channel-by-channel drilling is limited to the minimum pitch of 300 µm for 100 µm diameter through holes in 6.3 mm thickness fused silica, which could be reduced by using segmented drilling technique to mitigate impact by neighbouring channels.
4. Debris removal can be enhanced using de Laval air nozzle enabling 100 µm diameter and 8.5 mm depth cavities in fused silica, which is more than 8 times deeper compared to drilling without additional airflow.
5. Bottom-up processing using nanosecond pulses (4 or 11 ns) results in similar surface quality (chipping above 20 µm) and milling rate, and slightly higher milling efficiency compared to the GHz burst of the similar duration.

References

[1] C. Yu, S. Wu, Y. Zhong et al., "Application of Through Glass Via (TGV) Technology for Sensors Manufacturing and Packaging," *Sensors 2024, Vol. 24,* Vol. 24, pp. 171, 2023, doi:10.3390/S24010171.

[2] Q. Xu, D. Fang, X. Zhang et al., "Etch the borosilicate glass to form a straight through-glass-via based on the FLACE technology," *Journal of Micromechanics and Microengineering*, Vol. 32, pp. 055008, 2022, doi:10.1088/1361-6439/AC628E.

[3] L.A. Hof, J.A. Ziki, L.A. Hof et al., "Micro-Hole Drilling on Glass Substrates—A Review," *Micromachines (Basel).*, Vol. 8, 2017, doi:10.3390/MI8020053.

[4] S. Kim, J. Kim, Y.H. Joung et al., "Optimization of selective laser-induced etching (SLE) for fabrication of 3D glass microfluidic device with multi-layer micro channels," *Micro and Nano Systems Letters*, Vol. 7, pp. 15, 2019, doi:10.1186/S40486-019-0094-5.

[5] V. Tomkus, M. Mackevičiūtė, J. Dudutis et al., "Laser-machined two-stage nozzle optimised for laser wakefield acceleration," *J. Plasma Phys.*, Vol. 90, pp. 965900102, 2024, doi:10.1017/S0022377824000059.

[6] Y. Lu, Y.F. Li, G. Wang et al., "Femtosecond Laser Fabrication of Microchannels in Transparent Hard Materials," *Adv. Mater. Technol.*, Vol. 8, pp. 2300015, 2023, doi:org/10.1002/admt.202300015.

[7] J. Dudutis, G. Račiukaitis, E. Daknys et al., "Quality and flexural strength of laser-cut glass: classical top-down ablation versus water-assisted and bottom-up machining," *Opt. Express*, pp. 4564–4582, 2022, doi:10.1364/OE.447143.

[8] X. Zhao, Y.C. Shin, "Femtosecond laser drilling of high-aspect ratio microchannels in glass," *Appl. Phys. A Mater. Sci. Process.*, Vol. 104, pp. 713–719, 2011, doi:10.1007/S00339-011-6326-Z/METRICS.

[9] R.R. Gattass, E. Mazur, "Femtosecond laser micromachining in transparent materials," *Nat. Photonics*, Vol. 2, pp. 219–225, 2008, doi:10.1038/NPHOTON.2008.47.

[10] P. Balage, G. Bonamis, M. Lafargue et al., “Advances in Femtosecond Laser GHz-Burst Drilling of Glasses: Influence of Burst Shape and Duration,” *Micromachines (Basel).*, Vol. 14, pp. 1158, 2023, doi:10.3390/MI14061158.

[11] K. Mishchik, R. Kling, R. Beuton et al., “Improved laser glass cutting by spatio-temporal control of energy deposition using bursts of femtosecond pulses,” *Opt. Express*, Vol. 25, pp. 33271–33282, 2017, doi:10.1364/OE.25.033271.

[12] R.L. Sutherland, D.G. Mclean, S. Kirkpatrick, Handbook of Nonlinear Optics, Second Edition, Marcel Dekker, New York, 2003, doi:10.1201/9780203912539.

[13] I.N. Zavestovskaya, P.G. Eliseev, O.N. Krokhin et al., “Analysis of the nonlinear absorption mechanisms in ablation of transparent materials by high-intensity and ultrashort laser pulses,” *Appl. Phys. A.*, Vol. 92, pp. 903–906, 2008, doi:10.1007/S00339-008-4609-9.

[14] M. Ams, D.J. Little, M.J. Withford, Femtosecond-laser-induced refractive index modifications for photonic device processing, in: N.A. Vainos (Ed.), Laser Growth and Processing of Photonic Devices, Woodhead Publishing, 2012: pp. 305–332, doi:10.1533/9780857096227.3.305.

[15] S.J. Mihailov, “Femtosecond Laser-Inscribed Fiber Bragg Gratings for Sensing Applications,” *Opto-Mechanical Fiber Optic Sensors: Research, Technology, and Applications in Mechanical Sensing*, pp. 137–174, 2018, doi:10.1016/B978-0-12-803131-5.00006-4.

[16] C. Kerse, H. Kalaycloĝ Lu, P. Elahi et al., “Ablation-cooled material removal with ultrafast bursts of pulses,” *Nature*, Vol. 537, pp. 84–88, 2016, doi:10.1038/nature18619.

[17] Pierre Balage, “Gap materials interaction with femtosecond lasers in GHz-burst mode,” pp. 255, 2024. https://theses.hal.science/tel-04730713 (accessed June 25, 2025).

[18] S. Schwarz, S. Rung, C. Esen et al., “Enhanced ablation efficiency using GHz bursts in micromachining fused silica,” *Opt. Lett.*, Vol. 46, pp. 282–285, 2021, doi:10.1364/ol.415959.

[19] E. Audouard, E. Mottay, “High efficiency GHz laser processing with long bursts,” *International Journal of Extreme Manufacturing*, Vol. 5, pp. 015003, 2023, doi:10.1088/2631-7990/ACA79F.

[20] L. Zubauskas, E. Markauskas, P. Šleiniūtė et al., “Classical top-down fused silica milling with a femtosecond laser using different laser pulse burst regimes,” *J. Manuf. Process.*, Vol. 155, pp. 820–830, 2025, doi:10.1016/J.JMAPRO.2025.10.054.

[21] M. Sun, U. Eppelt, C. Hartmann et al., “Numerical analysis of laser ablation and damage in glass with multiple picosecond laser pulses,” *Opt. Express*, Vol. 21, pp. 7858–7867, 2013, doi:10.1364/OE.21.007858.

[22] H. Le, P. Penchev, A. Henrottin et al., “Effects of Top-hat Laser Beam Processing and Scanning Strategies in Laser Micro-Structuring,” *Micromachines (Basel).*, Vol. 11, pp. 221, 2020, doi:10.3390/MI11020221.

[23] A. Tuennermann, S. Nolte, J. Limpert, “Femtosecond vs. Picosecond Laser Material Processing,” *Laser Technik Journal*, Vol. 7, pp. 34–38, 2010, doi:10.1002/LATJ.201090006.

[24] S. Nikumb, Q. Chen, C. Li et al., “Precision glass machining, drilling and profile cutting by short pulse lasers,” *Thin Solid Films*, pp. 216–211, 2005, doi:10.1016/J.TSF.2004.08.136.

[25] B.C. Seok, J.P. Jung, “Recent Progress of TGV Technology for High Performance Semiconductor Packaging,” *Journal of Welding and Joining*, Vol. 42, pp. 155–164, 2024, doi:10.5781/JWJ.2024.42.2.2.

[26] A. Butkutė, T. Baravykas, J. Stančikas et al., “Optimization of selective laser etching (SLE) for glass micromechanical structure fabrication,” *Opt. Express*, Vol. 29, pp. 23487–23499, 2021, doi:10.1364/OE.430623.

[27] J. Zhang, K. Obata, K. Ozasa et al., “Rapid Manufacturing of Glass-Based Digital Nucleic Acid Amplification Chips by Ultrafast Bessel Pulses,” *Small Science*, Vol. 4, 2024, doi:10.1002/SMSC.202300166.

[28] P. Balage, M. Lafargue, T. Guilberteau et al., “Comparative Study of Percussion Drilling in Glasses with a Femtosecond Laser in Single Pulse, MHz-Burst, and GHz-Burst Regimes

and Optimization of the Hole Aspect Ratio," *Micromachines (Basel).*, Vol. 14, pp. 1754, 2023, doi:10.3390/MI14091754.

[29] J. Lopez, I. Manek-Hönninger, C. Hönninger et al., "Percussion drilling in glasses and process dynamics with femtosecond laser GHz-bursts," *Opt. Express*, Vol. 30, pp. 12533–12544, 2022, doi:10.1364/OE.455553.

[30] M.K. Bhuyan, F. Courvoisier, P.A. Lacourt et al., "High aspect ratio nanochannel machining using single shot femtosecond Bessel beams," *Appl. Phys. Lett.*, Vol. 97, pp. 81102, 2010, doi:10.1063/1.3479419/339875.

[31] Y. Zhang, T. Koike, R. Yoshizaki et al., "Ultrahigh-speed laser drilling of transparent materials via transient electronic excitation," *Sci. Adv.*, Vol. 11, pp. 4436, 2025, doi:10.1126/SCIADV.ADV4436.

[32] V. Tomkus, V. Girdauskas, J. Dudutis et al., "High-density gas capillary nozzles manufactured by hybrid 3D laser machining technique from fused silica," *Opt. Express*, pp. 27965–27977, 2018, doi:10.1364/OE.26.027965.

[33] J.M. Liu, "Simple technique for measurements of pulsed Gaussian-beam spot sizes," *Opt. Lett.*, Vol. 7, pp. 196, 1982, doi:10.1364/OL.7.000196.

[34] "MISUMI | Configurable Components | Distributor & Manufacturer," n.d. https://us.misumi-ec.com/ (accessed January 19, 2026).

[35] M. Sadauskas, V. Vrubliauskaitė, E. Kvietkauskas et al., "Laser-induced microscale copper trace deposition on glass and PET substrates," *Opt. Laser Technol.*, Vol. 183, pp. 112355, 2025, doi:10.1016/J.OPTLASTEC.2024.112355.

[36] V. Stankevič, K. Ratautas, D. Andriukaitis et al., "Electronics on any surface," *PhotonicsViews*, Vol. 22, pp. 26–29, 2025, doi:10.1002/PHVS.202500014.

[37] N. Hodgson, H. Allegre, A. Starodoumov et al., "Femtosecond Laser Ablation in Burst Mode as a Function of Pulse Fluence and Intra-Burst Repetition Rate," *JLMN-Journal of Laser Micro/Nanoengineering*, Vol. 15, 2020, doi:10.2961/jlmn.2020.03.2014.

[38] D. Metzner, P. Lickschat, C. Kreisel et al., "Study on laser ablation of glass using MHz-to-GHz burst pulses," *Applied Physics A*, Vol. 128, pp. 637, 2022, doi:10.1007/s00339-022-05776-7.

STIKLO APDIRBIMAS NUO APATINĖS BANDINIO PUSĖS ULTRATRUMPŲJŲ LAZERIO IMPULSŲ MHz/GHz PAPLIŪPOMIS

Aleksandras Kondratas

Magistro baigiamasis darbas

Lazerinė technologija

Vilniaus universitetas, fizikos fakultetas

Vadovas – Dr. Juozas Dudutis

Vilnius, 2026

Santrauka

56 puslapiai, 39 paveikslai, 6 lentelės, 38 literatūros šaltiniai.

Siekiant padidinti efektyvumą, gali būti naudojamos lazerinės papliūpos, sudarytos iš ultratrumpų impulsų, kurių pasikartojimo dažnis yra MHz arba GHz. Šiuose režimuose keli mažesnės energijos impulsai pirmiausia įkaitina medžiagą arba sukuria defektus, taip sumažindami abliacijos slenkstį ir leisdami vėlesniems impulsams efektyviau šalinti medžiagą. Didėjant impulsų skaičiui GHz papliūpoje, dielektrikų abliacijos mechanizmas kinta nuo medžiagos sublimacijos prie paviršiaus skilinėjimo ir fragmentacijos, todėl medžiaga šalinama efektyviau.

Šio darbo tikslas buvo ištirti lydyto kvarco apdirbimą iš apačios į viršų naudojant įvairias papliūpas. Buvo formuojamos ir analizuojamos 100 µm skersmens ertmės.

Apdirbimas naudojant MHz impulsų papliūpas sudarė negilias ertmes, todėl buvo neefektyvus. Kai MHz impulsų pakete buvo naudojami daugiau nei du impulsai, dauguma ertmių buvo nesėkmingai suformuotos dėl ertmėse susikaupusių abliacijos produktų.

Naudojant GHz papliūpas, apdirbimo efektyvumas didėjo didėjant impulsų skaičiui papliūpoje iki 21 impulso, po kurio pradėjo mažėti. Didžiausias apdirbimo efektyvumas buvo pasiektas naudojant 21 impulsą pakete, kurio vertė buvo 201±15 $\mu m^3/\mu J$. Tačiau didėjantis impulsų skaičius taip pat blogino apdirbimo kokybę, didindamas ištrupėjimą ir šoninių sienelių šiurkštumą. Bandinio apatinėje pusėje nuskilimai padidėjo nuo < 5 µm iki ~25 µm, kai impulsų skaičius GHz papliūpoje buvo padidintas nuo 4 iki 21.

Apdirbimas iš apačios į viršų naudojant nanosekundinius impulsus (4 ir 11 ns) lėmė panašią paviršiaus kokybę (nuskilimai > 20 µm), panašų apdirbimo greitį ir šiek tiek didesnį apdirbimo efektyvumą nei panašios trukmės GHz papliūpos.

Siekiant pagerinti nuolaužų pašalinimą, buvo naudojami oro srauto purkštukai, kurie padidino pasiekiamą ertmių gylį. Efektyviausias nuolaužų pašalinimas buvo pasiektas naudojant de Lavalio oro purkštuką, kuris leido kvarciniame stikle suformuoti 100 µm skersmens ir 8,5 mm gylio ertmes. Šis gylis yra daugiau nei aštuonis kartus didesnis nei pasiektas be papildomo oro srauto.

BOTTOM-UP PROCESSING OF GLASS USING MHz/GHz BURSTS OF ULTRASHORT LASER PULSES

Aleksandras Kondratas

Master's thesis

Laser technology

Vilnius University, Faculty of Physics

Supervisor – Dr. Juozas Dudutis

Vilnius, 2026

Summary

56 pages, 39 figures, 6 tables, 38 references.

Milling efficiency can be improved by utilising burst modes consisting of ultrashort pulses with MHz or GHz repetition rates. In these regimes, several lower-energy pulses initially heat the material or create defects, reducing the ablation threshold and allowing subsequent pulses to remove material more efficiently. As the number of pulses in a GHz burst increases, the ablation mechanism in dielectrics shifts from material sublimation to surface cracking and fragmentation, resulting in more efficient material removal.

The aim of this work was to investigate bottom-up milling of fused silica using various ultrashort laser burst modes. Cavities with a diameter of 100 µm were milled and analysed.

Milling with MHz bursts produced shallow cavities and was therefore inefficient. When more than two pulses were used in a MHz burst, most cavities failed due to fused debris accumulating inside the cavities.

For GHz bursts, the milling efficiency increased with the number of pulses in a burst up to 21 pulses, after which it began to decrease. The highest milling efficiency, 201±15 $\mu m^3/\mu J$, was achieved with 21 pulses per burst. However, increasing the number of pulses also reduced processing quality by increasing chipping and sidewall roughness. On the bottom side of the sample, chipping increased from less than 5 µm to approximately 25 µm when the number of pulses in a GHz burst was increased from 4 to 21.

Bottom-up processing using nanosecond pulses (4 and 11 ns) resulted in similar surface quality (chipping > 20 µm), a comparable milling rate, and slightly higher milling efficiency than GHz bursts of similar duration.

Airflow nozzles were used to improve debris removal, which increased the achievable cavity depth. Debris removal was enhanced the most when using a de Laval air nozzle, enabling the fabrication of cavities with a 100 µm diameter and 8.5 mm depth in fused silica. This depth is more than eight times greater than that achieved without additional airflow.

Approbation

Collection of presentations and papers prepared during the master's studies.

Presentations related to the thesis:

[1] A. Kondratas, J. Dudutis, P. Gečys, "Bottom-up drilling of glass using bursts of ultrashort laser pulses", *international conference Open Readings 2026*, Vilnius, Lithuania, oral presentation

Presentations not related to the thesis:

[1] A. Kondratas, J. Dudutis, P. Gečys, "Glass scribing with Bessel beam using MHz bursts", *internation conference Open Readings 2025*, Vilnius, Lithuania, poster presentation, Prof. Piskarskas Award for Best Poster Presentation on Photonics and Laser Technologies

[2] A. Kondratas, J. Dudutis, "Greitos lazerinio beselio pluošto skenavimo sistemos tyrimas ir taikymas medžiagų apdirbimui", *LMT studentų tyrimų semestrų metu konferencija „Naujoji karta su LMT"*, Vilnius, Lithuania, oral presentation

Publications not related to the thesis:

[1] M. Mackevičiūtė, A. Kondratas, J. Dudutis et al., "Ultrafast soda-lime glass scribing via self-filamentation of laser bursts," *J. Manuf. Process.*, Vol. 150, pp. 740–750, 2025, doi:10.1016/J.JMAPRO.2025.06.047.

[2] J. Dudutis, A. Kondratas, P. Gečys, "Polarization-Dependent Laser-Assisted Cutting of Glass Using a Nondiffractive Beam in the MHz Burst Regime," *ACS Photonics*, Vol. 12, pp. 3706–3716, 2025, doi:org/10.1021/acsphotonics.5c00679.